JOURNAL OF GEOPHYSICAL RESEARCH, VOL. 111, D13203, doi:10.1029/2005JD006687, 2006

Optical properties of deep glacial ice at the South Pole

M. Ackermann,[1] J. Ahrens,[2] X. Bai,[3] M. Bartelt,[4] S. W. Barwick,[5] R. C. Bay,[6] T. Becka,[2] J. K. Becker,[4] K.-H. Becker,[7] P. Berghaus,[8] E. Bernardini,[1] D. Bertrand,[8] D. J. Boersma,[9] S. Böser,[1] O. Botner,[10] A. Bouchta,[10] O. Bouhali,[8] C. Burgess,[11] T. Burgess,[11] T. Castermans,[12] D. Chirkin,[13] B. Collin,[14] J. Conrad,[10] J. Cooley,[9] D. F. Cowen,[14] A. Davour,[10] C. De Clercq,[15] C. P. de los Heros,[10] P. Desiati,[9] T. DeYoung,[14] P. Ekström,[11] T. Feser,[2] T. K. Gaisser,[3] R. Ganugapati,[9] H. Geenen,[7] L. Gerhardt,[5] A. Goldschmidt,[13] A. Groß,[4] A. Hallgren,[10] F. Halzen,[9] K. Hanson,[9] D. H. Hardtke,[6] T. Harenberg,[7] T. Hauschildt,[3] K. Helbing,[13] M. Hellwig,[2] P. Herquet,[12] G. C. Hill,[9] J. Hodges,[9] D. Hubert,[15] B. Hughey,[9] P. O. Hulth,[11] K. Hultqvist,[11] S. Hundertmark,[11] J. Jacobsen,[13] K. H. Kampert,[7] A. Karle,[9] M. Kestel,[14] G. Kohnen,[12] L. Köpke,[2] M. Kowalski,[1] K. Kuehn,[5] R. Lang,[1] H. Leich,[1] M. Leuthold,[1] I. Liubarsky,[16] J. Lundberg,[10] J. Madsen,[17] P. Marciniewski,[10] H. S. Matis,[13] C. P. McParland,[13] T. Messarius,[4] Y. Minaeva,[11] P. Miočinović,[6] R. Morse,[9] K. Münich,[4] R. Nahnhauer,[1] J. W. Nam,[5] T. Neunhöffer,[2] P. Niessen,[3] D. R. Nygren,[13] P. Olbrechts,[15] A. C. Pohl,[10] R. Porrata,[6] P. B. Price,[6] G. T. Przybylski,[13] K. Rawlins,[9] E. Resconi,[1] W. Rhode,[4] M. Ribordy,[12] S. Richter,[9] J. Rodríguez Martino,[11] H.-G. Sander,[2] S. Schlenstedt,[1] D. Schneider,[9] R. Schwarz,[9] A. Silvestri,[5] M. Solarz,[6] G. M. Spiczak,[17] C. Spiering,[1] M. Stamatikos,[9] D. Steele,[9] P. Steffen,[1] R. G. Stokstad,[13] K.-H. Sulanke,[1] I. Taboada,[6] O. Tarasova,[1] L. Thollander,[11] S. Tilav,[3] W. Wagner,[4] C. Walck,[11] M. Walter,[1] Y.-R. Wang,[9] C. H. Wiebusch,[7] R. Wischnewski,[1] H. Wissing,[1] and K. Woschnagg[6]

Received 19 September 2005; revised 20 January 2006; accepted 15 March 2006; published 8 July 2006.

[1] We have remotely mapped optical scattering and absorption in glacial ice at the South Pole for wavelengths between 313 and 560 nm and depths between 1100 and 2350 m. We used pulsed and continuous light sources embedded with the AMANDA neutrino telescope, an array of more than six hundred photomultiplier tubes buried deep in the ice. At depths greater than 1300 m, both the scattering coefficient and absorptivity follow vertical variations in concentration of dust impurities, which are seen in ice cores from other Antarctic sites and which track climatological changes. The scattering coefficient varies by a factor of seven, and absorptivity (for wavelengths less than ~450 nm) varies by a factor of three in the depth range between 1300 and 2300 m, where four dust peaks due to stadials in the late Pleistocene have been identified. In our absorption data, we also identify a broad peak due to the Last Glacial Maximum around 1300 m. In the scattering data, this peak is partially masked by scattering on residual air bubbles, whose contribution dominates the scattering coefficient in shallower ice but vanishes at

[1]Deutsches Elektronen-Synchrotron, Zeuthen, Germany.
[2]Institute of Physics, University of Mainz, Mainz, Germany.
[3]Bartol Research Institute, University of Delaware, Newark, Delaware, USA.
[4]Institute of Physics, University of Dortmund, Dortmund, Germany.
[5]Department of Physics and Astronomy, University of California, Irvine, California, USA.
[6]Department of Physics, University of California, Berkeley, California, USA.
[7]Department of Physics, University of Wuppertal, Wuppertal, Germany.
[8]Science Faculty CP230, Université Libre de Bruxelles, Brussels, Belgium.
[9]Department of Physics, University of Wisconsin, Madison, Wisconsin, USA.
[10]Division of High Energy Physics, Uppsala University, Uppsala, Sweden.
[11]Department of Physics, Stockholm University, Stockholm, Sweden.
[12]Faculty of Sciences, University of Mons-Hainaut, Mons, Belgium.
[13]Lawrence Berkeley National Laboratory, Berkeley, California, USA.
[14]Department of Physics and Astronomy, Pennsylvania State University, University Park, Pennsylvania, USA.
[15]Dienst ELEM, Vrije Universiteit Brussel, Brussels, Belgium.
[16]Blackett Laboratory, Imperial College, London, UK.
[17]Department of Physics, University of Wisconsin, River Falls, Wisconsin, USA.

0148-0227/06/2005JD006687$09.00

∼1350 m where all bubbles have converted to nonscattering air hydrates. The wavelength dependence of scattering by dust is described by a power law with exponent -0.90 ± 0.03, independent of depth. The wavelength dependence of absorptivity in the studied wavelength range is described by the sum of two components: a power law due to absorption by dust, with exponent -1.08 ± 0.01 and a normalization proportional to dust concentration that varies with depth; and a rising exponential due to intrinsic ice absorption which dominates at wavelengths greater than ∼500 nm.

Citation: Ackermann, M., et al. (2006), Optical properties of deep glacial ice at the South Pole, *J. Geophys. Res.*, *111*, D13203, doi:10.1029/2005JD006687.

1. Introduction

[2] In the natural sciences, it is not uncommon that advances in one field are pertinent to understanding processes in other, seemingly unrelated, fields. The optical properties of glacial ice are of relevance to scientific endeavors beyond the most obviously related fields of optics and glaciology. For wavelengths between ∼200 and ∼400 nm, glacial ice is the most transparent solid known [*Askebjer et al.*, 1995, 1997a; *Price*, 2006]. The optical attenuation of naturally occurring ice, particularly for solar radiation, is used in modeling of the radiative energy balance of the Earth's surface. It also plays an important role in efforts, fueled by the discovery of stratospheric ozone depletion, to estimate the levels of damaging UV radiation that reach biological organisms, such as marine biota in and under sea ice [*Trodahl and Buckley*, 1990; *Perovich*, 2001]. Similarly, but with opposite implications, attempts are made within the Snowball Earth hypothesis [*Hoffman et al.*, 1998] to estimate the amount of photosynthetically active radiation (PAR) that could have penetrated the frozen surface of the tropical oceans, part of an Earth-blanketing ice cover posited to have existed at least twice during the neo-Proterozoic period ∼700 million years ago, to sustain biological life under the ice through photosynthesis [*Warren et al.*, 2002]. In natural glacial ice, variations with depth in concentrations of insoluble dust particles and ash as read out by optical methods track climate changes [*Bay et al.*, 2004].

[3] Light propagation in deep ice at the South Pole is also relevant to the field of neutrino astrophysics. Knowledge of the optical properties of the ice is essential for operation of the AMANDA (Antarctic Muon and Neutrino Detector Array) [*Andrés et al.*, 2001] and IceCube [*Ahrens et al.*, 2004a] neutrino telescopes. These arrays of photomultiplier tubes are embedded deep in the glacial ice to identify high-energy neutrinos via the detection of Cherenkov light generated by secondary particles produced in neutrino-nucleon interactions near the detector. To measure the trajectories and energies of these interaction products (predominantly muons and electromagnetic cascades from electrons) from the detected Cherenkov photons, one needs to understand and take into account the effects of scattering and absorption of light at wavelengths in the visible and near ultraviolet.

[4] To carry out optical measurements deep in the glacial ice at the South Pole, we developed remote optical techniques that are complementary to standard glaciological methods such as ice coring. Light from pulsed and steady light sources buried in the ice was recorded with the AMANDA sensors and used to extract scattering and absorption parameters. Our measurements based on pulsed in situ light sources are unique in that they enable us to distinguish between scattering and absorption, even though the two are correlated in the data. Before our work, optical oceanographers and glaciologists often used transmissometers that recorded loss of light from a collimated beam. They generally used the term attenuation, without distinguishing loss by scattering from loss by absorption, which in some compilations led to overestimates of absorptivity. Optical measurements on laboratory-grown pure ice suffered from the same inherent difficulties in separating absorption from scattering in beam attenuation measurements, compounded by uncertainties related to having a block of ice a few meters long to measure absorption lengths many times larger.

[5] Measurements of optical properties of South Pole ice have been previously reported for depths between 800 and 1000 m. An AMANDA precursor detector at these relatively shallow depths was used to measure scattering and absorption in ice with high concentrations of air bubbles that resulted in very short scattering lengths [*Askebjer et al.*, 1997a, 1997b]. As pressure increases with depth, air bubbles compress and eventually become unstable against a transition from the gas phase to the solid air-hydrate clathrate phase [*Miller*, 1969]. Because the rate of transformation is slow, bubbles and air hydrate crystals coexist over a depth range of several hundred meters [*Price*, 1995]. The phase boundary depends on both temperature and pressure. Fortuitously, the refractive indices of air hydrate and of normal ice are almost identical [*Uchida et al.*, 1995], as a consequence of which light passes through an air hydrate crystal with almost no scattering. The AMANDA scattering results led to predictions [*Price and Bergström*, 1997b], later confirmed [*Price et al.*, 2000], that all bubbles have transformed into the solid phase at ∼1500 m, and that at greater depths the optical properties in the visible region depend almost solely on the concentration of dust in the ice. Using data collected with an AMANDA array at 1500 to 2000 m in the early calibration stages, a number of properties of South Pole ice have been published: a first estimate of age versus depth [*Price et al.*, 2000] based on a comparison with data from Antarctic ice cores collected at Vostok [*Petit et al.*, 1999] and Dome Fuji [*Watanabe et al.*, 1999] stations; the temperature profile down to 2350 m [*Price et al.*, 2002] from which the ice temperature at bedrock was estimated to be −9°C; and a weak temperature dependence of absorptivity at 532 nm [*Woschnagg and Price*, 2001] which is in agreement with measurements on

a range of transparent solids over many orders of magnitude in wavelength. In the present paper we present comprehensive results on scattering and absorption for wavelengths from the near ultraviolet through the visible and for depths down to 2350 m. The same principles apply to the optical properties of glacial ice in Greenland and at other Antarctic locations.

2. Theoretical Considerations

[6] The optical sensors in AMANDA are sensitive to light with wavelengths between 300 and 600 nm, enabling us to study optical properties of Antarctic ice in that wavelength interval. The short-wavelength limit is set by the transmission properties of the glass pressure spheres housing the photomultiplier tubes. The limit at long wavelengths is set by the decline in photocathode quantum efficiency.

2.1. Scattering

[7] Light scattering in deep ice is described by scattering on microscopic scattering centers, such as submillimeter-sized air bubbles and micron-sized dust grains [*Price and Bergström*, 1997b]. The general case for scattering of electromagnetic radiation off small particles was first rigorously treated by Gustav Mie by application of classical electromagnetic theory starting with Maxwell's equations [*Mie*, 1908]. A "particle" here is a closed region, for example a small mass of material, with a refractive index that differs from the refractive index of its surroundings. For simplicity, Mie scattering assumes spherical particles, and for our application we can safely ignore interference effects since the average distance between scattering particles is large compared to the wavelength. We typically record light that has been scattered several times. A general property of photon multiple scattering [*Kirk*, 1999] is that the average cosine of the light field after n scattering events, $\langle \cos\theta \rangle_n$, can be expressed in terms of the average cosine of the angle θ for a single scatter, the anisotropy $\langle \cos\theta \rangle$, by the relation $\langle \cos\theta \rangle_n = \langle \cos\theta \rangle^n$. The interpretation of the anisotropy is straightforward: if $\langle \cos\theta \rangle > 0$, scattering is preferentially forward; if $\langle \cos\theta \rangle = 0$, scattering is forward-backward symmetric. Isotropic scattering is a special case of forward-backward symmetry. The geometric scattering length, λ_s, also referred to as the scattering mean free path, is the average distance between scatters. Given that the scattering angle follows a scattering function $p(\theta)$ and the average scattering angle is expressed in $\langle \cos\theta \rangle$, we can define an effective scattering length λ_e by adopting the definition of the transport mean free path, which is the length scale over which randomization occurs, in the limit of many scatters, when scattering is not isotropic. For isotropic scatters, $\lambda_e = \lambda_s$, but for strongly forward peaked anisotropic scatters, as is the case here, λ_e is significantly greater than λ_s. We estimate λ_e by a statistical argument common in radiative transfer theory [e.g., *Chandrasekhar*, 1950]. Consider a beam of light propagating in a scattering medium without absorption. On average, the light is scattered at successive steps of length λ_s, and the average angle between two steps is $\langle \cos\theta \rangle$. After each step i the effective light transport advances another $\lambda_s \langle \cos\theta \rangle^i$ along the initial direction. By summing the projections of all n steps in a long path onto the direction of the first step, we arrive at the total effective length of light transport:

$$\lambda_e = \lambda_s \sum_{i=0}^{n} \langle \cos\theta \rangle^i \tag{1}$$

which for large n becomes

$$\lambda_e = \frac{\lambda_s}{1 - \langle \cos\theta \rangle}. \tag{2}$$

Hence when light propagates through a turbid medium the center of the photon cloud moves along the incident direction at a decreasing pace until it comes to a halt at one λ_e from the point of injection. The effective scattering length is thus for anisotropic scattering what the geometric scattering length is for isotropic scattering. With the AMANDA array, we operate in a regime of multiple scattering (but not yet diffusion) and this precludes us from measuring λ_s and $\langle \cos\theta \rangle$ independently. Technically, then, the introduction of the effective scattering length is more a practical way of reducing the number of independent variables (from two, λ_s and $\langle \cos\theta \rangle$, to one, λ_e). It is often more convenient to discuss scattering in terms of the reciprocal of λ_e, the effective scattering coefficient

$$b_e = \frac{1}{\lambda_e}. \tag{3}$$

[8] We made detailed numerical calculations based on Mie theory [*Bohren and Huffman*, 1983] to estimate the effects of scattering off randomly distributed micron-sized particles on the propagation of light through dusty ice. As input to these calculations, we used a dust model described by four components (we followed the treatment by *He and Price* [1998]). The main component was insoluble mineral grains, contributing strongly to both scattering and absorption. Sea salt crystals were the most strongly scattering component, but they contributed very little to absorption. Liquid acid drops (mainly sulfuric acid) also had negligible absorption. Soot was highly absorbing but it was the least scattering dust component. In our calculations, individual components were described by the following characteristics: mean (modal radius r) and width (geometric standard deviation) of the lognormal distribution of particle sizes; depth-dependent density and mass concentration; and complex refractive index. We used the estimated South Pole values derived by *He and Price* [1998] from Antarctic ice core measurements, except for the mass concentrations which we updated with estimates based on more recent ice core data from Vostok [*Petit et al.*, 1999] and Dome Fuji [*Watanabe et al.*, 1999]. Adopting the procedure by *He and Price* [1998], the core mass concentrations were scaled with the ratios of concentrations in surface snow samples of comparable ages from the different sites, assuming these ratios are valid at all depths corresponding to the same time periods, and were then translated to the South Pole with the age versus depth curve from *Price et al.* [2000]. We also modified the summing over components and weighted the contribution from each of the four dust components with its

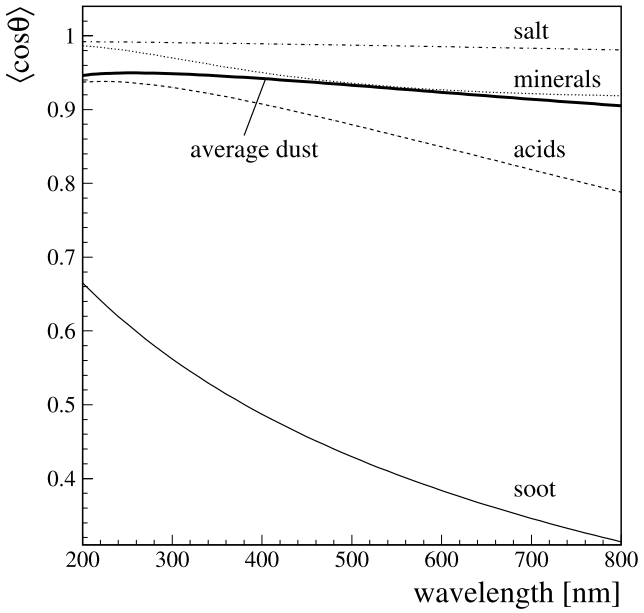

Figure 1. Wavelength dependence of $\langle \cos\theta \rangle$, where θ is the scattering angle, from Mie scattering calculations for a realistic mixture of four dust components: mineral grains, sea salt, acids, and soot. We used a canonical value of 0.94 for our photon propagation simulations, representing an average over relevant wavelengths.

scattering coefficient instead of its concentration. The lognormal size distributions had means ranging from ~12 nm for soot to ~400 nm for sea salt, and geometric standard deviations around 2. The calculations showed that for light between 300 and 600 nm scattering off dust has a wavelength dependence that can be described by a power law

$$b_e \propto \lambda^{-\alpha} \tag{4}$$

with an exponent α close to 1 which depends strongly on grain size and thus on dust composition. For comparison, in the case of Rayleigh scattering ($\lambda \gg r$) the wavelength dependence is λ^{-4} (and scattering is forward-backward symmetric), while geometric scattering ($\lambda \ll r$) is independent of wavelength (provided absorption is so weak that $r \ll$ absorption length). Below we present measurements of α made in ice at depths greater than 1500 m, and we discuss results from a search for a possible dependence of α on depth.

[9] Figure 1 shows the wavelength dependence of $\langle \cos\theta \rangle$ from our Mie scattering calculations. For a four-component sample with the estimated South Pole component mixture the average $\langle \cos\theta \rangle$ was 0.94, with only a weak dependence on wavelength. We used 0.94 as a canonical value in our measurements of optical parameters and investigated the sensitivity of our results to the value of $\langle \cos\theta \rangle$ as part of the study of systematics (see discussion in section 6). For scattering off air bubbles, which exist in the shallower glacial ice with sizes down to a few tens of micrometers [*Barkov and Lipenkov*, 1984; *Lipenkov*, 2000], the value of $\langle \cos\theta \rangle$ is close to 0.75 [*Askebjer et al.*, 1995].

[10] The Mie scattering calculations were also used to study the scattering probability density function $p(\theta)$ (called the phase function in radiative transfer theory). For a single particle size, the scattering angle distribution exhibited wavelength-dependent spectral structure, and for some sizes had a considerable back-scattering component. However, summing over realistic lognormal size distributions smoothed the distribution (Figure 2). Since in our case scattering was strongly forward peaked with $\langle \cos\theta \rangle$ close to 1, we chose as scattering function the Henyey-Greenstein approximation [*Henyey and Greenstein*, 1941], first introduced to describe the observed diffuse intensity pattern of stellar radiation caused by forward peaked scattering off interstellar dust clouds:

$$p(\cos\theta) = \frac{1}{2} \frac{1 - \langle \cos\theta \rangle^2}{\left(1 + \langle \cos\theta \rangle^2 - 2\langle \cos\theta \rangle \cos\theta\right)^{3/2}}. \tag{5}$$

For our purposes, the advantages of this function were that it was characterized by only one parameter, the average cosine of the scattering angle θ, and that it was easily integrated and inverted for use in our Monte Carlo simulations of photon propagation which we used to measure the optical properties of ice with data from pulsed light sources. In Figure 2, the normalized Henyey-Greenstein function, expressed both as $p(\cos\theta)$ and as $p(\theta) = p(\cos\theta)\sin\theta$, is compared with the scattering angle distribution from our modeling of dust with $\langle \cos\theta \rangle = 0.94$. In our experimental setup, distances between emitter-receiver pairs were greater than a few scattering lengths, which prevented us from measuring the scattering function in situ.

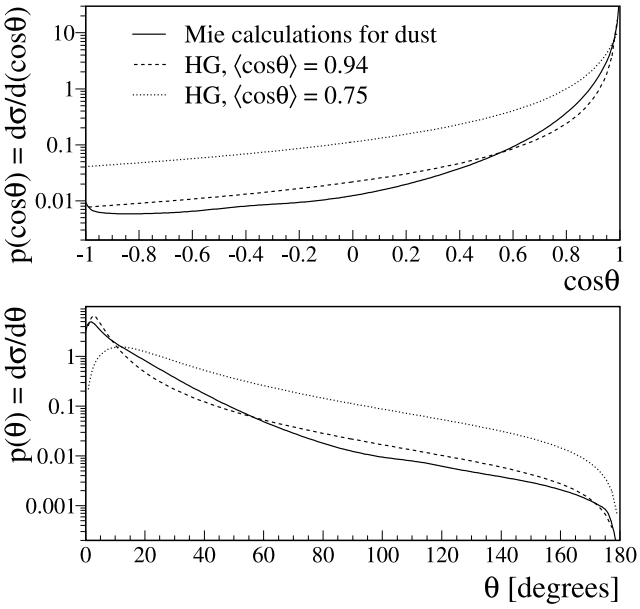

Figure 2. Scattering probability density function. Mie scattering calculations for dust yield a strongly forward peaked scattering angle distribution which can be approximated with the single-parameter Henyey-Greenstein (HG) function. The scattering function for $\langle \cos\theta \rangle = 0.75$ is valid for bubbles in ice [*Price and Bergström*, 1997b].

2.2. Absorption

[11] The absorptive strength of a medium is often described by the absorption length λ_a, the distance at which the survival probability drops to $1/e$, or its reciprocal, the absorption coefficient (or absorptivity)

$$a = \frac{1}{\lambda_a} \tag{6}$$

which is related to the imaginary (absorptive) part of the index of refraction n by

$$a = \frac{4\pi \mathrm{Im}(n)}{\lambda} \tag{7}$$

where λ is the wavelength of the light. *Price and Bergström* [1997b] introduced an empirical model to describe the wavelength dependence of absorptivity of ice in the far ultraviolet through infrared (IR). In their three-component model, absorptivity is parameterized as

$$a(\lambda) = A_U e^{-B_U \lambda} + C_{dust} \lambda^{-\kappa} + A_{IR} e^{-\lambda_0/\lambda} \tag{8}$$

where the second term is due to insoluble dust particles in the ice, and the two exponentials characterize light absorption by the ice itself and are independent of dust content. The first term describes an "Urbach tail" [*Urbach*, 1953], a steep exponential decrease in absorptivity that occurs at wavelengths slightly longer than that corresponding to an electronic band-gap energy which depends weakly on temperature. A fit to measurements of ice absorption in the far-ultraviolet (180–186 nm) by *Minton* [1971] yielded $A_U = 8.7 \times 10^{39}$ m^{-1} and $B_U = 0.48$ nm^{-1}, placing the Urbach tail for ice just shortward of 200 nm. The third term is an approximation of the exponential rise in the red and infrared due to molecular absorption by pure ice. Absorptivity in this regime exhibits spectral structure due to different modes of H_20 molecular stretching, bending and vibration. For South Pole ice, the IR exponential dominates for wavelengths longer than ~500 nm. In the intermediate range, between ~200 and ~500 nm, pure ice is believed to be extremely transparent and absorption is dominated by impurities in the form of insoluble dust. Modeling of absorption caused by dust with Mie theory [*He and Price*, 1998] showed that the wavelength dependence can be described by a power law whose exponent depends only weakly on dust grain size and thus composition (since the four components have different size distributions), so in our analysis we assumed that κ is independent of depth. For a given composition and size distribution, C_{dust} is proportional to dust concentration, which varies with depth and carries information about climate.

[12] In measurements made in South Pole ice at depths between 800 and 1000 m [*Askebjer et al.*, 1997a], absorptivity was found to be much lower than expected from measurements on laboratory-grown ice and lake ice. Absorption lengths in the violet, where absorptivity is a minimum, were found to exceed 200 m. There are two reasons for the discrepancy between laboratory and in situ measurements. In the 300–500 nm interval, absorption is dominated by impurities, and glacial ice at the South Pole is far cleaner than lake ice [*Sauberer*, 1950] and probably also chemically purer than the laboratory ice (freshly grown from purified water) used for measurements of optical properties [*Grenfell and Perovich*, 1981; *Perovich and Govoni*, 1991]. In addition, previous investigators had measured attenuation of a collimated beam, in a geometry where more light was lost by scattering than by absorption. *Price and Bergström* [1997a] have argued that, since the laboratory ice measurements in this wavelength range fit a λ^{-4} line about two orders of magnitude higher than what is expected for Rayleigh scattering in pure ice, the laboratory data were dominated by Rayleigh scattering on crystalline defects in the form of chemical impurities concentrated as discontinuous strings of nanoscale beads in decorated dislocations.

[13] Depths between 800 and 1000 m correspond to ages in the onset of the Holocene, a geological time period spanning the last 11,000 years, which is characterized by a mild global climate and low dust concentrations in the atmosphere. Near the bottom of the 800–1000 m interval, the absorptivity increased with dust concentration signaling the approach to the Last Glacial Maximum, a time ~23,000 years ago corresponding to a depth of ~1300 m in South Pole ice. The combination of low dust concentrations in the Holocene ice and the fact that the shortest wavelength used in the early measurements at 800–1000 m was 410 nm [*Askebjer et al.*, 1997a] prevented a precise measurement of the expected power law wavelength dependence for dust absorption, since the third term in equation (8) dominated over the (second) dust term. A wavelength dependence of λ^{-2}, derived from Mie modeling of dust, was therefore assumed. In the present analysis we included data at shorter wavelengths, recorded in deeper and therefore older and dustier ice, and we measured the power law exponent κ with high precision and investigated its depth dependence.

3. Experimental Setup and Data

[14] The AMANDA neutrino telescope comprises 677 optical modules (OM) arranged on 19 vertical strings (Figure 3), embedded deep in the glacial ice at the South Pole. During construction, the strings were lowered into 60 cm-wide hot-water-drilled holes and fixed permanently into place as the water refroze. Each OM consists of one photomultiplier tube (PMT) mounted in a 30 cm outer diameter glass pressure sphere. After using first-generation spheres with a cutoff in transmittance (<5%) close to 340 nm for the first 4 (inner) strings, second-generation spheres with better transmission properties in the UV (~65% at 340 nm) were used for the subsequent 15 strings. The bulk of the array spans depths between 1500 and 2000 m, with three strings extending 350 m above and below this range, mainly for calibration purposes. South Pole bedrock is at a depth of 2820 m. PMT pulses were transmitted to the data acquisition system located at the surface by optical fibers and by electrical cables (also used to supply power). The PMTs were operated at high gain (typically 10^9) to make it possible to distinguish single-photoelectron pulses from dark noise after attenuation over 2 km-long cables. For each pulse, its leading edge time, pulse width, and peak amplitude were recorded. The resolution for individual photon hit times was 5 ns.

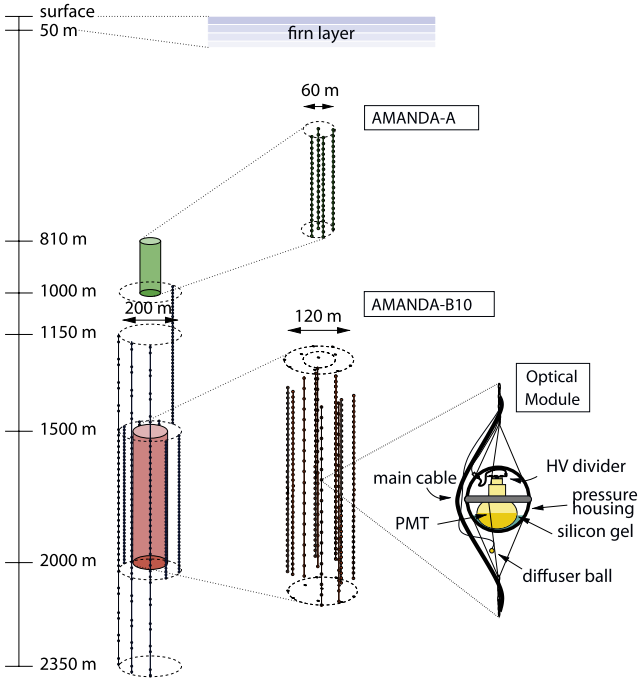

Figure 3. Schematic view of the AMANDA neutrino telescope buried deep in glacial ice at the South Pole. The optical properties presented in this paper were measured using in situ light sources embedded in the array below 1150 m depth. Measurements in shallower ice, using the AMANDA-A detector, have been reported previously by *Askebjer et al.* [1995, 1997a, 1997b].

[15] The relative position of every optical module in the array, and of every calibration light source, was known to within less than 1 m after geometry calibration with two independent methods. The first method did not rely on any in situ optical data: a string's position in the horizontal plane (on the surface) was measured with a survey of the borehole location; the vertical positions of the optical modules on a string were determined by first measuring the depth of the string with a pressure sensor deployed with the string in the water-filled hole, and then applying the known OM spacings along the string; and data from sensors in the drill head provided a profile of the hole in terms of deviations from the vertical, which were then applied to the horizontal positions of individual OMs. In the second method the relative positions of the strings (horizontal distances and relative depths) were verified, or corrected, with pulsed YAG laser data (described below) from at least five locations on every string, by fitting the propagation time of unscattered photons recorded at several receivers on all neighboring strings. Modeling of glacial flow based on the South Pole ice temperature profile [*Price et al.*, 2002] suggests that the top 2000 m of the glacier moves as a rigid volume, below which the flow rate steadily decreases with depth so that the deepest OMs, at ~2350 m, possibly lag behind by up to 1 m per year. However, all data below 2000 m used in this analysis were recorded within one year of the installation of the three deep strings (see Figure 3) so the geometry could safely be considered static throughout the duration of the measurements.

3.1. Pulsed Light Sources

[16] A number of pulsed light sources at different wavelengths were included on the optical module strings for detector calibration purposes. In this analysis, data from the following four source types were used (their main characteristics are listed in Table 1):

[17] 1. A frequency-doubled Nd:YAG laser emitting 4 ns-wide light pulses at 532 nm was located in the counting house on the ice surface. The light was fed through optical fibers down to diffuser balls at known locations on every string throughout the detector array, and emitted in an isotropic intensity pattern. The laser was coupled to one fiber at a time. Dispersion in the multimode fibers introduced pulse broadening that depended on fiber length, resulting in an average pulse width of 15 ns at the time of injection into the ice. On the inner ten strings, the diffuser balls were located outside the glass spheres of the optical modules; on the outer strings, the diffuser balls were inside the spheres. The laser was operated at repetition rates of 50–100 Hz, depending on the ability of the data acquisition system to process given photon fluxes.

[18] 2. Two nitrogen lasers, emitting 337 nm light, were deployed on separate strings near the center of the detector.

Table 1. Characteristics of In Situ Light Sources Embedded With the AMANDA Neutrino Telescope

Light Source	Wavelength Spectrum		Emission Pattern	Pulse Width, ns	Pulse Rate, Hz	Maximum Number of Photons (Injected Into Ice)[a]
	Peak, nm	FWHM, nm				
Pulsed sources						
YAG laser	532	<0.1	isotropic	15[b]	50–100	10^8–10^9/pulse
Blue LED flashers	470	30	vertical cos θ	6; τ = 18[c]	100[d]	10^9/pulse
UV LED flashers	370	12	tilted cos θ	6; τ = 18[c]	64–256	3×10^9/pulse
Nitrogen lasers	337	0.2	vertical cos θ	3	6.8, 20	2×10^{12}/pulse
Steady sources						
UV Module	313	10	vertical cos θ	continuous	continuous	5×10^{11}/s
Rainbow Module	340–560[e]	20	vertical cos θ	continuous	continuous	$\sim 10^{11}$/s[f]

[a]These are estimates for the brightest settings; the output could be reduced for all sources.
[b]The width depended on the length of the optical fiber; 15 ns was the average for a 2 km fiber.
[c]The first number is the FWHM of the leading edge; τ is the time constant of the exponential tail.
[d]The blue flashers fired at 1 kHz, but the data acquisition rate was artificially reduced.
[e]The range of the monochromator was 200–800 nm; the effective range for data recorded with the AMANDA OMs was limited to 340–560 nm by the glass transmittance and the PMT quantum efficiency.
[f]This is an order-of-magnitude estimate for 460 nm; the output increased approximately tenfold from 340 to 560 nm.

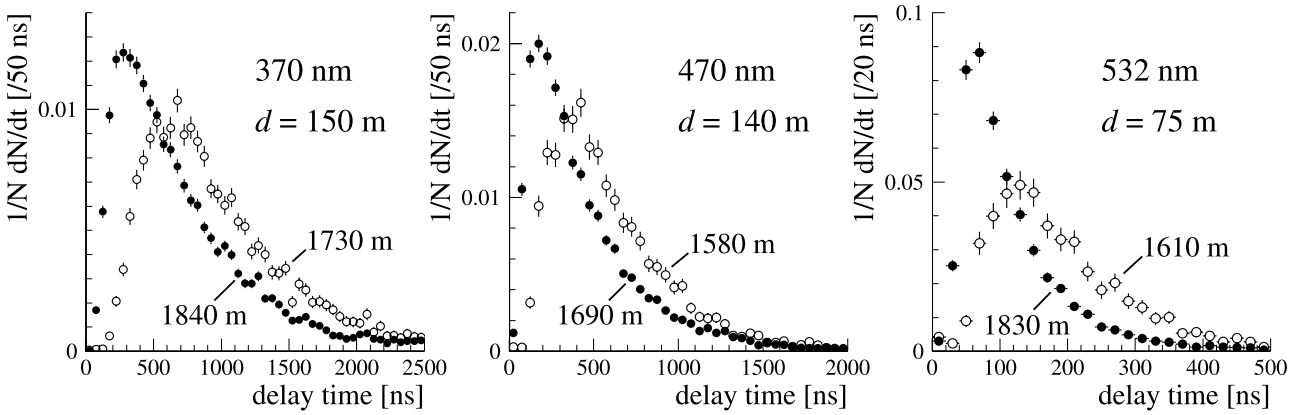

Figure 4. Photon delay time distributions for light from pulsed sources at three wavelengths. For each source type are shown two distributions recorded at the same distance d but at two depths where the ice has different optical properties. The broader distributions with steeper tails (open circles) indicate dustier ice with stronger scattering and absorption.

The lasers were mounted in first-generation glass pressure spheres, which absorbed roughly 97% of the photons at this wavelength. Both laser modules had two filters mounted on the outside of their sphere: a UV filter to reject any fluorescence generated by the laser light passing through the glass, and a diffusive filter causing an upward peaked intensity pattern roughly proportional to the cosine of the angle from vertical. The lasers fired at 6.8 Hz and 20 Hz, respectively, with a pulse width of 3 ns FWHM. Each source was equipped with a variable attenuator, controlled from the surface, which provided up to seven decades of attenuation. At the brightest setting, each pulse from one of the 200 μJ lasers injected approximately 2×10^{12} photons into the ice. Because of laser aging, the pulse energy decreases by an estimated 30% every two years.

[19] 3. Eight optical modules were equipped with blue "flashers," each containing six LEDs at 470 nm (30 nm FWHM) mounted on a circular board inside the upper hemisphere of the OM's glass sphere. The blue flasher modules were deployed at different depths on two of the three longer detector strings with instrumented cable lengths of 1200 m (see Figure 3). Each surface-mount LED (Nichia NSCB100A) had an intensity pattern roughly proportional to cos θ, and was mounted with its symmetry axis pointing vertically up. Each 6-LED flasher emitted pulses of up to 10^9 photons, with a 6 ns (FWHM) risetime and an exponential tail with a time constant $\tau = 18$ ns. The blue flashers fired at 1 kHz, but the data acquisition rate was artificially reduced to ~100 Hz with a 10 ms veto after each trigger to reduce the effects of deadtime caused by the processing of the very large photon fluxes.

[20] 4. Similar flashers, emitting UV light from GaN LEDs (Nichia NSHU550A) peaking at 370 nm (12 nm FWHM), were part of 41 optical modules on one of the strings located on the perimeter of the 19-string array [*Ackermann et al.*, 2006]. The UV flashers used the same electronics board as the blue flashers, with six LEDs regularly spaced around the perimeter, pointing outward and up at a 45° angle from the horizontal, giving a broad angular pattern and pulses with the same time profile as the blue flashers. Both pulse rate and amplitude were controlled from the surface. At the highest amplitude setting, each UV flasher generated pulses that injected 3×10^9 photons into the ice, after the glass had absorbed ~15% of the light.

[21] During recording of data generated by any of the pulsed sources, readout of the optical module array was triggered by the emitted pulses to avoid diluting the data sample with events not caused by the sources (mostly due to muons, created in cosmic ray interactions in the atmosphere, which were sufficiently energetic to reach detector depths) and to get accurate pulse start times for photon propagation time measurements. For the YAG laser, pulses from a photodiode sampling a small fraction of the laser output at the surface were used for triggering. For the nitrogen lasers and the LED flashers, large pulses seen in the closest optical module (usually 10–20 m away), and therefore with very sharp risetimes, were used for triggering. Photon arrival times, recorded for all optical modules in the array, were calibrated to compensate for cable delays and amplitude-dependent delays in the data acquisition electronics. For every recorded arrival time, the similarly calibrated pulse start time was subtracted together with the prompt propagation time d/c_{ice} (corresponding to unscattered travel over a distance d) to yield photon delay time distributions.

[22] If a receiver recorded more than one photon in an event, only the earliest time was retained. This procedure was justified by two features of the experimental setup that resulted in a more accurate arrival time determination for the first photon than for later photons. First, pulse broadening in the cables sometimes caused overlapping electrical pulses, which made it difficult to resolve the later pulses and determine their leading edges. Second, for every receiver only the largest pulse amplitude was recorded in multiphoton events, and since this amplitude in a majority of cases was associated with the first pulse, the time calibration was more accurate for the first photon.

[23] Examples of photon delay time distributions are shown in Figure 4 for data from pulsed sources at three wavelengths. For each wavelength, the two distributions shown in Figure 4 were recorded at the same distance, horizontally from the source, but with the emitter-receiver pairs located at two depths where the ice has different

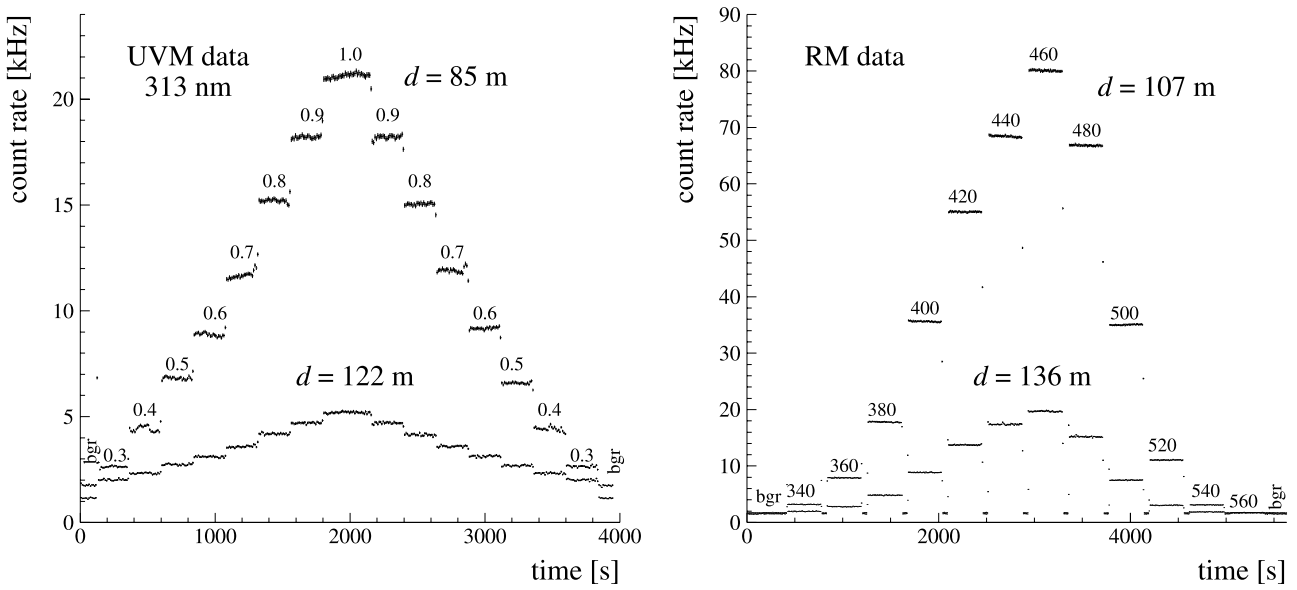

Figure 5. Recorded count rates in runs with the two steady light sources, the 313 nm UV Module and the variable-wavelength Rainbow Module, for two typical receivers at different distances. Each data point shows the average count rate over 10 s. For the UVM data, the intensity was varied in 4 min intervals, with an additional 2 min at maximum brightness. For the RM data, the wavelength was varied between 340 and 560 nm in steps of 20 nm, with the source turned off for 1 min between every 6 min period at a fixed wavelength. Anomalous points in the transitions were ignored in the analysis. The periods marked "bgr" were recorded with the source disabled.

optical properties. The distributions recorded in dustier ice are broader, because of stronger scattering, and have steeper slopes in the tails, indicative of more absorption.

3.2. Steady Light Sources

[24] To measure the optical properties of the ice over a wider wavelength range than was accessible with the pulsed sources, two very bright steady light sources were also deployed with the optical module strings:

[25] 1. The Ultra-Violet Module (UVM) contained a 20 W Xenon arc lamp whose light was reflected and focused on a 313 ± 5 nm filter and passed through a diffusion filter. The light source was housed in a custom-made aluminum cylinder with a 3.8 cm UV transmitting acrylic window on one end cap to ensure high (∼50%) transmittance of the light into the ice. The UVM was deployed at ∼1850 m and oriented with the window facing up so that the peak intensity was along the vertical axis. The light source was powered by AC from the surface, activating a special igniter circuit in the module, and the light intensity was controlled with a variable autotransformer. The output from the UVM at its brightest setting was estimated to be on the order of 5×10^{11} photons per second.

[26] 2. The Rainbow Module (RM) was a steady light source whose output wavelength could be varied between 340 and 560 nm, with a resolution of 20 nm FWHM. Its light source was a halogen lamp, mounted in an aluminum reflector for higher light yield in the UV. Direct and reflected light from the lamp was focused by a series of lenses and beamed through a grating monochromator controlled from the surface. The characteristics of the monochromator were chosen to optimize throughput, by using larger slits, at the expense of resolution. The RM light source assembly was housed in a second-generation glass sphere with high transmittance above 340 nm (∼65% increasing to ∼90% longward of 400 nm). The RM was deployed on a string at 60 m radius from the central string, at a depth of ∼1850 m, and with the symmetry axis of the light intensity pattern oriented upward. From the data, we estimated that the RM emitted on the order of 10^{11} photons per second at 460 nm.

[27] Like the pulsed nitrogen lasers, the two steady sources were run with high voltage supplied from the surface. This generated high levels of electromagnetic noise which contaminated data from OMs on the same string as the source beyond usefulness, so that only data on neighboring strings could be used for this analysis. Data generated by the steady sources were recorded with an array of counters attached to the main data acquisition system on the surface, with one counter for each optical module. Each counter recorded the number of hits above threshold in 0.5 s periods, where a hit was either an electrical pulse from the PMT in the OM or a noise pulse generated in the electronics or through cross talk in the cable, and the count rate was then averaged over 10 s intervals. Figure 5 shows recorded rates, N, for two receivers at different distances from the source, both for UVM data at varying brightness settings and for RM data at varying wavelengths. The settings were kept constant for periods of between 4 and 6 min, seen in Figure 5 as distinct steps of near-constant rate marked with the relative brightness (for the UVM) or wavelength (for the RM). To measure the background (dark noise) rates, data were also recorded for a few minutes before and after the source was turned on in each run. The rates were then

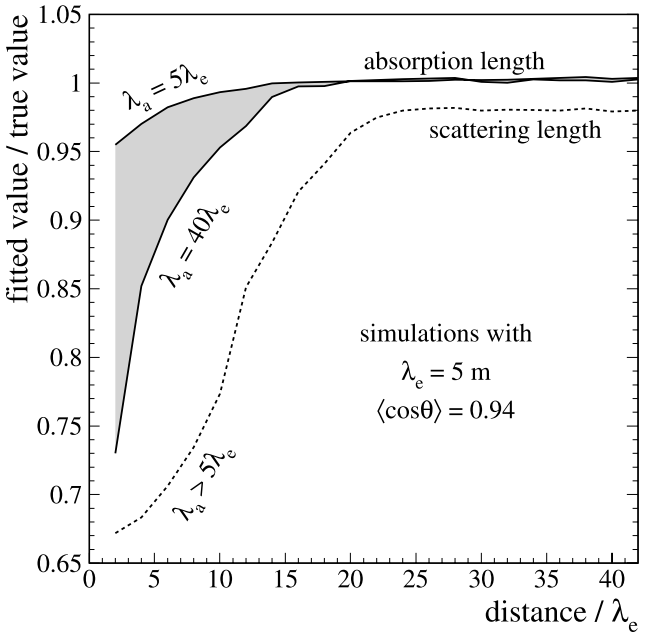

Figure 6. When absorption is considerably weaker than scattering, the optical parameters obtained from a fit of the Green's function for a random walk with absorption, equation (9), to simulated photon arrival time distributions converge with the true values at distances greater than $\sim 20\lambda_e$ (for λ_e, independent of λ_a) and $\sim 15\lambda_e$ (for λ_a). Scattering anisotropy causes the scattering length to be slightly underestimated in the fit.

averaged for each period, after subtracting the background rate in the run, B, yielding mean rates, $\langle N \rangle$, with standard deviations, σ_N. During some periods, the rate fluctuations were dominated by instabilities in the light source (for example, in the first period with 0.4 relative UVM brightness in Figure 5). Steady source data were therefore retained for further analysis only for periods in which $\sigma_N < \sqrt{\langle N \rangle + B}$, discarding less than 4% of the data because of source instabilities.

4. Analysis Techniques

4.1. Measuring Optical Properties With Pulsed Light Sources

[28] Light propagation to a receiver at a distance $d \gg \lambda_e$, sufficiently far from a source for the photons to scatter many times, is described by a random walk with absorption [*Askebjer et al.*, 1997a]. If absorption is considerably weaker than scattering, it can be added to the statistical random walk treatment as a survival probability which decreases exponentially with path length. The arrival times t of photons emitted from an isotropic source at $t = 0$ are then, in this diffusive regime, distributed according to the Green's function

$$u(d,t) = \frac{1}{(4\pi Dt)^{3/2}} \exp\left(-\frac{d^2}{4Dt}\right) \exp\left(-\frac{tc_{\text{ice}}}{\lambda_a}\right) \qquad (9)$$

where $D = c_{\text{ice}}\lambda_e/3$ is the diffusion constant, $c_{\text{ice}} = c/n_g$ is the velocity of light in ice, and n_g is the group velocity refractive index, which depends on the wavelength of the light [*Price and Woschnagg*, 2001]. If λ_a is comparable to λ_e, a large fraction of the photon flux will be absorbed before it becomes fully diffusive and the arrival times cannot be described by equation (9). We performed simulations of photon propagation in a turbid and absorbing medium which showed that the above random walk description is valid for distances greater than approximately $20\lambda_e$ (Figure 6), provided λ_a is substantially greater than λ_e. At closer distances, the formula gave a poor description of arrival times (Figure 7), particularly for early photons which had only suffered a few scatters, shifting the leading edge to noncausally early times (see example in Figure 9). The scattering anisotropy caused the effective scattering length obtained from the analytical fits to be systematically underestimated by ~2%, independent of $\langle \cos\theta \rangle$ in the range 0.60–0.99.

[29] In the precursor detector located at depths between 800 and 1000 m, scattering was dominated by submillimeter-sized residual air bubbles which are not absorbing. In data from pulsed in situ light sources, emitter-receiver distances were tens of meters and the effective scattering length was less than one meter [*Askebjer et al.*, 1995], making the recorded light diffusive. In addition, absorption lengths were on average two orders of magnitude greater than the effective scattering length. Under these circumstances, the optical properties could be extracted analytically from photon arrival time distributions with the random walk expression above. In the deeper AMANDA detector, bubbles have effectively disappeared by converting to nonscattering air hydrate crystals. At these depths, scattering by dust dominates, significantly increasing the effective scattering length in comparison with the bubbly ice, and

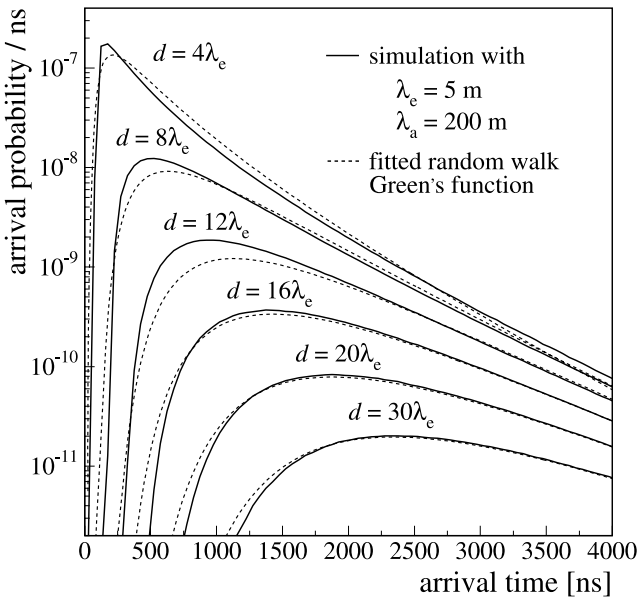

Figure 7. Green's function for a random walk with absorption fitted to simulated photon arrival time distributions recorded at different distances from an isotropic source. The tail of the distribution, which is dominated by absorption, is described at shorter distances than the leading edge and the peak, which are dominated by scattering.

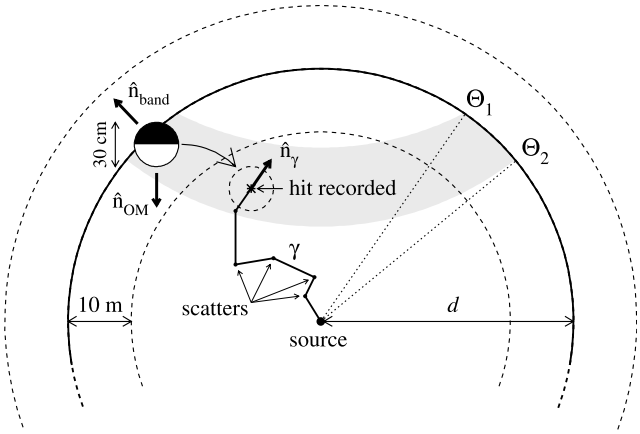

Figure 8. Principles for the photon propagation Monte Carlo simulation used to fit timing data from pulsed light sources. The propagation time of photons (γ) generated at the origin were recorded at every crossing of a spherical shell. Each shell was divided into eighteen bins in zenith angle. The angular acceptance of the optical modules was taken into account by weighting the arrival times according to the photon incidence angle.

absorption lengths are shorter because of higher concentrations of dust. Although some receivers in the deeper detector are sufficiently far from the emitters for the light to be diffusive, most distances are too short for photon arrival times to be described analytically with the random walk function. Instead, we measured the optical properties by using a Monte Carlo simulation to model the propagation of photons through ice with given optical parameters, and then adjusted these parameters until photon timing distributions from our simulations agreed with the in situ data.

[30] In the Monte Carlo, photons were generated at the origin at time $t = 0$ with a given distribution of initial directions (for example, isotropic) and were then propagated through a medium with homogeneous scattering and absorption parameters, λ_e^{MC} and λ_a^{MC}. Each photon was scattered after consecutive steps l_i, randomly drawn from an $\exp(-l/\lambda_s)$ probability distribution, by an angle randomly drawn from a Henyey-Greenstein function with $\langle\cos\theta\rangle = 0.94$. To sample the photon flux at intervals small enough to justify a linear interpolation between sampling points, the space around the virtual light source was interspersed with concentric spheres, centered on the point of generation and spaced 10 m apart (Figure 8), serving as detection surfaces. Since neither the OM acceptance nor (necessarily) the light source was isotropic, the resulting angular dependence was accounted for by dividing each spherical shell into eighteen 10° bins in the zenith angle Θ (we used a right-handed Cartesian coordinate system collinear with the AMANDA coordinate system, in which z is pointing vertically up, and whose origin is 1730 m below the surface of the glacier, close to the geometric center of the array). For each of the resulting bins (or bands) a distribution of arrival times was constructed by recording the photon travel time at every shell crossing within the band. For a shell crossing occurring at time t, the probability to be recorded by a virtual OM (i.e., to generate a "hit") was

$$P_{\rm hit} = \frac{\epsilon_{\rm OM}\pi R_{\rm OM}^2\left[\dfrac{1-\hat{n}_\gamma\cdot\hat{n}_{\rm OM}}{2}\right]}{A_{\rm band}|\hat{n}_\gamma\cdot\hat{n}_{\rm band}|}\exp\left(-\frac{tc_{\rm ice}}{\lambda_a}\right) \qquad (10)$$

where $\epsilon_{\rm OM}$ is the overall detection efficiency for a spherical OM with radius $R_{\rm OM}$, $\hat{n}_\gamma$ is the photon direction at the time of recording, and $\hat{n}_{\rm OM} = (0,0,1)$ is the OM direction (defined as the normal to the PMT photocathode surface, always facing straight down). Each band spanning zenith angles from Θ_1 to Θ_2 on a shell with radius d was described by its area $A_{\rm band} = 2\pi d^2|\cos\Theta_1 - \cos\Theta_2|$ and normal vector $\hat{n}_{\rm band}$ at the point where the photon intersected the shell. The angular acceptance of the optical modules was accounted for by the expression in square brackets, which was derived from a simple model that approximated the real efficiency: the upper hemisphere was assumed to be opaque and the lower hemisphere completely transparent. The relative acceptance was then 100% for photons from straight below, 0% for photons from straight above, and, for zenith angles in between, proportional to the fraction of projected area that was transparent from that angle. Absorption was taken into account by assigning a weight to each hit on the basis of the photon's path length, $l = tc_{\rm ice}$, instead of eliminating it from the simulation at an age drawn from the corresponding $\exp(-l/\lambda_a)$ survival probability distribution. With this importance sampling technique, the tails of the time distributions, corresponding to old photons, accumulated statistics faster.

[31] Simulated time distributions $f(t,d_i,\Theta_j)$ were generated in a lattice of spatial points, defined by their distance d_i and zenith angle Θ_j relative to the emitter, by summing the probabilities for all hits within a time bin with width Δt (typically 10 ns),

$$f(t) = \sum_{N[t,t+\Delta t]} P_{\rm hit}, \qquad (11)$$

with a statistical error $f(t)/\sqrt{N}$ on the contents of that bin. Before a hit was added to the appropriate histogram, its recorded time was randomly smeared by a Gaussian with $\sigma = 5$ ns to simulate uncertainties in the time calibration. From the resulting histograms, delay time distributions could be calculated at any distance from an emitter by interpolation between the two closest shells.

[32] Every delay time distribution from in situ data was compared with a simulated (MC) distribution at the corresponding distance and angle relative to the emitter by computing the chi-square of the comparison,

$$\chi^2 = \sum_i \frac{\left(N_i^{\rm data} - N_i^{\rm MC}\right)^2}{\left(\sigma_i^{\rm data}\right)^2 + \left(\sigma_i^{\rm MC}\right)^2}, \qquad (12)$$

where i ran over the contiguous set of nonempty bins that included the peak of the data distribution. By definition, the simulated distributions described the timing of single photons. Since for multiphoton data events we only used the time of the earliest photon, such distributions were

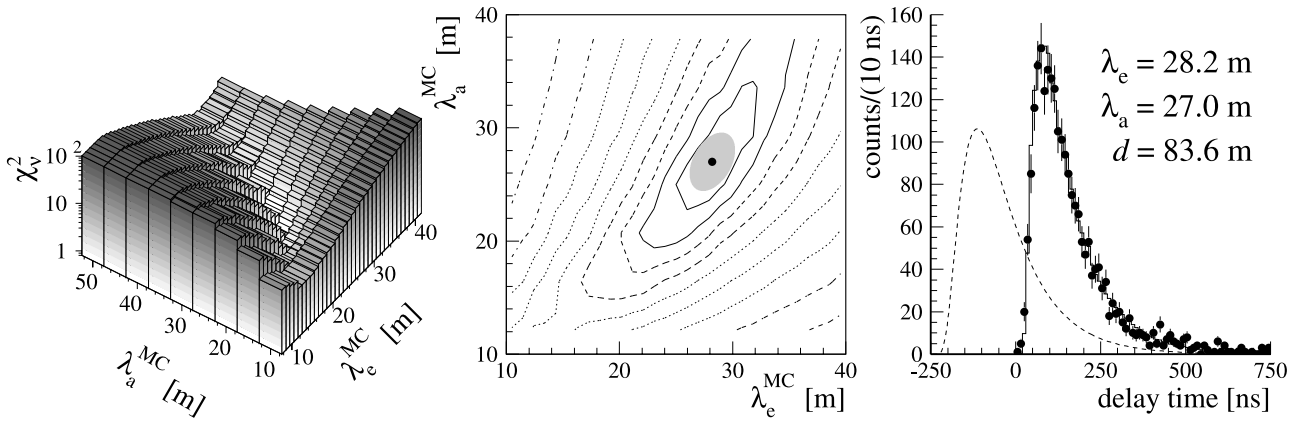

Figure 9. Example of a simulation-based fit to a recorded photon arrival time distribution from pulsed data at 532 nm. (left) Distribution of reduced χ^2 in λ_e-λ_a space from comparisons of the data distribution with simulations using different optical parameters. An elliptic paraboloid, equation (16), was fitted to the χ^2 surface near the minimum. (middle) Fitted minimum and the one-standard-deviation error ellipse. (right) Delay time distributions for data (points) and for simulation with the fitted parameters (histogram). A random walk Green's function with the same optical parameters (dashed curve) poorly describes the delay times at this distance.

artificially biased toward earlier times. To ensure that the data distributions could be compared directly with the simulated distributions, only data from receivers with an average number of photoelectrons $\langle N_{\rm pe}\rangle$ less than 0.2 were retained, meaning that they contained at least 90% single-photoelectron events. For the remaining fraction of multi-photoelectron events, the simulated distributions were reweighted to reflect the associated shift toward earlier times. For a Poissonian probability distribution with mean μ,

$$P(N_{\rm pe}) = \frac{\mu^{N_{\rm pe}} e^{-\mu}}{N_{\rm pe}!}, \tag{13}$$

it follows that

$$\mu = \langle N_{\rm pe}\rangle = -\ln P(0), \tag{14}$$

where $1 - P(0)$ is the occupancy of the receiver. To estimate $\langle N_{\rm pe}\rangle$ for a data distribution, we determined the occupancy from

$$1 - P(0) = \frac{N_{\rm data}}{N_{\rm fired}}, \tag{15}$$

where $N_{\rm fired}$ was the number of times the source had fired (taken as the number of events in the run triggered as described above) and $N_{\rm data}$ was the number of times the OM under consideration had recorded at least one hit (i.e., the number of events in the data distribution, since only the first hit was used). For each photon multiplicity $N_{\rm pe}$ from 1 to 10, $N_{\rm pe}$ delay times were randomly drawn from the single-photoelectron histogram and only the shortest of these was entered into a saturated histogram, until $P(N_{\rm pe})N_{\rm data}/(1 - P(0))$ entries had been added for that multiplicity. This correction worked well if the occupancy was less than ~20%, but gradually degraded with increasing $\langle N_{\rm pe}\rangle$ as the OM response was no longer purely Poissonian.

[33] We generated delay time distributions with the Monte Carlo simulation for a large number of combinations of optical parameters λ_e^{MC} and λ_a^{MC}, which were varied in small steps (typically 1 m in λ_e^{MC} and 5 m in λ_a^{MC}) over the expected range of values. Every delay time distribution from in situ data was compared with the (reweighted) simulated distribution corresponding to each combination (λ_e^{MC}, λ_a^{MC}) by computing the chi-square of the comparison with equation (12), resulting in a two-dimensional χ^2 grid in λ_e^{MC} and λ_a^{MC}. Close to the minimum, the shape of the grid was described by an elliptic paraboloid,

$$\chi^2 = \frac{2.3}{1-\rho^2}\left(\frac{\Delta_e^2}{\sigma_e^2} + \frac{\Delta_a^2}{\sigma_a^2} - \frac{2\rho\Delta_e\Delta_a}{\sigma_e\sigma_a}\right) + \chi^2_{\rm min} \tag{16}$$

where

$$\Delta_{e(a)} = \lambda_{e(a)}^{MC} - \lambda_{e(a)}, \tag{17}$$

characterized by six parameters: λ_e and λ_a are the best fit scattering and absorption lengths, σ_e and σ_a are their respective one-standard-deviation errors, ρ is the correlation between the parameters, and $\chi^2_{\rm min}$ is the χ^2 at the minimum. Figure 9 shows a χ^2 grid for a 532 nm delay time distribution at 84 m from the emitter and the error ellipse from a paraboloid fit near the minimum.

[34] Systematic uncertainties in the determination of the pulse start time were taken into account by introducing a time offset parameter t_0 that was allowed to vary freely in the fits. Hence each fit was sensitive only to the shape of the distribution, a function of distance, which was known to within less than one meter, and of scattering and absorption, but not to the absolute time or the normalization. The distribution of all fitted time offsets t_0 had a mean of 4 ns and a 10 ns standard deviation, verifying the validity of the pulse start time estimation.

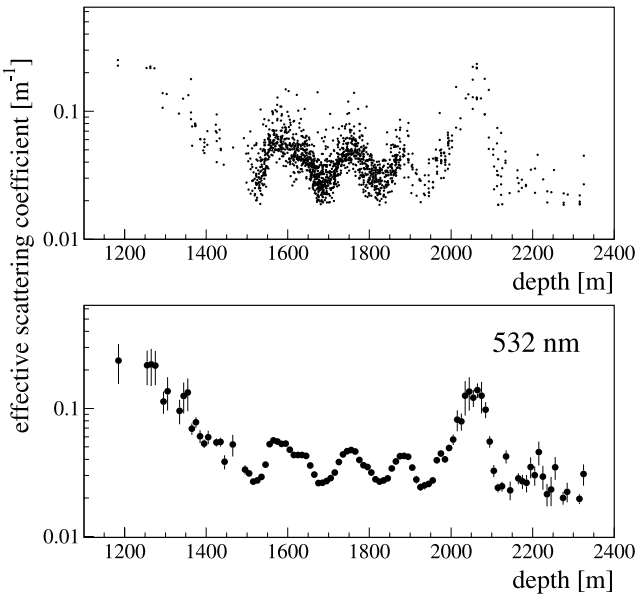

Figure 10. Depth profile for scattering at 532 nm. (top) All fitted effective scattering coefficients b_e (without statistical errors, for clarity) versus the average depth of emitter and receiver. (bottom) Weighted averages in 10 m depth bins. The error bars indicate one-standard-deviation errors in the means.

[35] Although scattering effects dominated the shapes of the leading edge and the peak in the time distributions and absorption largely determined the slope in the tail, the two parameters could not be cleanly separated, particularly since λ_e and λ_a were of the same order. In the timing fits this was manifested by a strong statistical correlation between the fitted scattering and absorption parameters. For the full data set, the distribution of fitted correlation coefficients ρ had a mean of 0.83, with only small variations between the data samples at different wavelengths, and a root-mean-square of 0.09.

[36] The measured optical parameters were sorted in 10 m depth bins, where the depth for each data point was the average depth of the emitter and the receiver. Only emitter-receiver pairs spaced less than 60 m apart vertically were used to ensure that the data predominantly probed thin horizontal slices of ice. Other selection criteria, such as high overall fit quality (i.e., a reduced χ^2 close to one), low fraction of multiphotoelectron events in the sample, and small relative statistical errors on the fitted parameters (indicating a successful fit), resulted in an average spacing of 15 m. In each depth bin, the optical parameters were averaged over all b_e (or a) in the bin, weighting each data point with its statistical error from the paraboloid fit. Averaging was performed on the coefficients rather than the lengths, since the former had Gaussian distributions in the bins. Figure 10 shows the resulting depth profile for scattering at 532 nm. Variations with depth in the optical properties could be resolved to within less than $\sim$10 m with this technique. The large variations in the scattering coefficient at depths greater than 1500 m are correlated with varying dust concentration and are discussed below.

4.2. Measuring Optical Properties With Steady Light Sources

[37] The optical ice properties were measured with data generated by the steady light sources through a fluence analysis, by measuring how the time-integrated photon fluxes recorded by the optical modules depended on their distances from the emitter. This technique was independent of simulations of photon propagation and thus did not require assumptions about the scattering function or $\langle \cos\theta \rangle$. Since both the data and the method were independent of those used with the pulsed technique, the fluence analysis provided complementary measurements and could be used for consistency checks and to study systematics.

[38] Although the Green's function for a random walk with absorption could not be used to fit photon timing data analytically, the formula is useful in being able to describe how the photon density varies with distance. For a steady light source, we integrate equation (9) over time, and find [*Askebjer et al.*, 1997a] that in the fully diffusive regime the photon fluence, in our experimental circumstances measured by the recorded OM count rate N, depends on distance d through

$$N(d \gtrsim 5\lambda_e) \propto \frac{1}{d} e^{-d/\lambda_p} \tag{18}$$

where we have introduced the propagation length

$$\lambda_p = \sqrt{\frac{\lambda_e \lambda_a}{3}} \tag{19}$$

to describe the combined effect of scattering and absorption over large distances. The propagation length differs from the commonly used attenuation length defined for beam attenuation experiments as $\lambda_{att} = 1/(a + b)$ where $b = 1/\lambda_s$. The latter describes the probability that a photon is removed from a beam by either scattering or absorption, whereas the propagation length is a useful parameter for diffusive photon transport from a point source. As before, we also define its reciprocal, the propagation coefficient

$$c_p = \frac{1}{\lambda_p} = \sqrt{3ab_e}. \tag{20}$$

For two receivers, A and B, at distances d_A and $d_B > d_A$ from an emitter, it follows from equation (18) that we can determine the average c_p for the ice between the two receivers from

$$c_p = -\frac{\ln(N_B d_B) - \ln(N_A d_A)}{d_B - d_A} = -\frac{\Delta \ln(Nd)}{\Delta d} \tag{21}$$

which means that the propagation coefficient can be measured locally through the decrease in count rate with distance, and does not depend on the properties of the ice between the emitter and the closest receiver (A). Equations (18) and (21) are valid closer to the emitter ($\sim 5\lambda_e$ away) than the random walk Green's function (which only fits time distributions at least $\sim 20\lambda_e$ away). Even if absorption were sufficiently weak to allow us to record pulsed data with high statistics at distances great enough to use equation (9) to fit

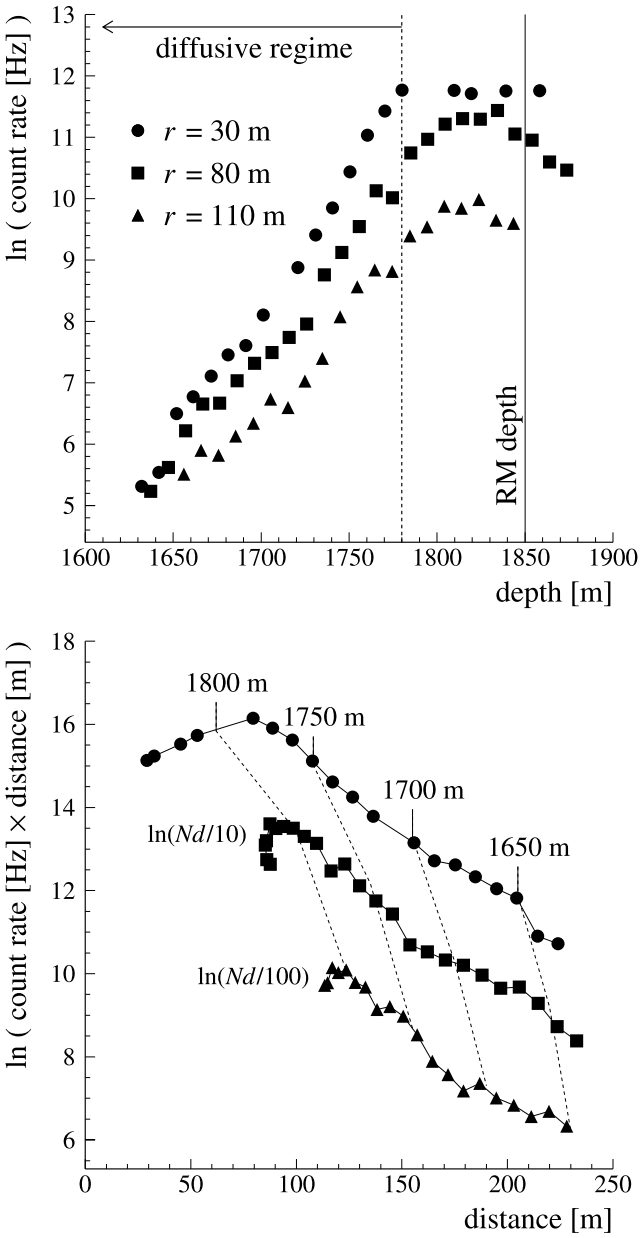

Figure 11. Rainbow Module (RM) data at 400 nm for receivers on three strings at different horizontal distances r from the emitter. (top) Rates ln(N) versus depth for all receivers. (bottom) The (rescaled) ln(Nd) versus distance d for the same receivers. The propagation coefficients c_p are given by the slopes between points in Figure 11 (bottom).

time distributions, the thin cylindrical shape of the array implies that the only receivers sufficiently far away are at least 350 m above (or below) the emitter. This means that the data would probe ice with strongly varying properties and the resulting optical parameters would be averages over that ice. The fluence analysis of steady data provides a way to probe the ice vertically without averaging over dust layers.

[39] Figure 11 shows photon count rates ln(N) as function of depth and ln(Nd) as function of distance for a 400 nm run with the Rainbow Module, located at a depth of ~1850 m. Data recorded on three strings at different horizontal distances from the source are compared. For the closest string, some of the counters saturated. Because of the strongly upward peaked intensity pattern, the count rates were highest 20–30 m above the RM, even 110 m away horizontally, and started to decrease for receivers that were closer in depth and below the source. As can be seen in Figure 11 (bottom), for the same distance from the source, receivers on different strings probed different layers of ice, which is seen as a difference in slope (and thus propagation coefficient c_p) for receivers on different strings but at the same distance.

[40] For every pair of receivers with a relatively small difference in their distances to the emitter ($\Delta d < 40$ m), and which were both located in ice with similar optical properties ($\Delta z < 20$ m, with $\langle \Delta z \rangle \approx 10$ m for the final data sample), the propagation coefficient c_p was determined with equation (21). To ensure that the recorded light was diffusive, receivers less than 80 m from the source were excluded, as well as receiver pairs that gave unphysical values $c_p < 0$ due to differences in detection efficiency between receivers. The steady source data were recorded with the 10-string array (AMANDA-B10 in Figure 3) which constitutes the inner core of the full 19-string array. The four innermost strings have 20 OMs each, at depths between 1550 and 1950 m, and are arranged in a cylindrical topology with one string at the center and three at a 30 m radius. The two upward pointing steady sources are located at the lower ends of two of the six strings that lie on a 60 m radius from the center of the array, and whose receivers are at depths between 1500 and 1850 m. Because of the thin cylindrical geometry of the array, the diffusive requirement was fulfilled only for receivers well above the source, and the fluence analysis was therefore restricted to depths less than ~1780 m.

[41] The overall efficiency ratio between first- and second-generation glass spheres, integrated over the effective wavelength spectrum, was 0.86, with a strong wavelength dependence in the near UV. In the fluence analysis, rates for the optical modules on the four inner strings were therefore rescaled with the wavelength-dependent transmittance ratio between the two glass types.

[42] After analysis of the full data set, and averaging c_p in 10 m depth bins, the depth dependence of the propagation coefficient (Figure 12) exhibited strong variations due to varying dust concentration (compare Figure 10), and the wavelength dependence closely followed the expected two-component shape in the transition between a power law due to dust absorption and an exponential rise in the red due to intrinsic ice absorption (compare equation (8)). For receivers on strings close to the emitter some of the data used in the analysis were not fully in the diffusive regime, and this introduced small systematic uncertainties that resulted in fluctuations from the smooth two-component shape in the wavelength dependence (e.g., see the points for 1765 m in Figure 12 (bottom)).

5. Results

5.1. Scattering

[43] We measured scattering as a function of depth with data from pulsed sources at four wavelengths. The depth dependence of the effective scattering coefficient is shown

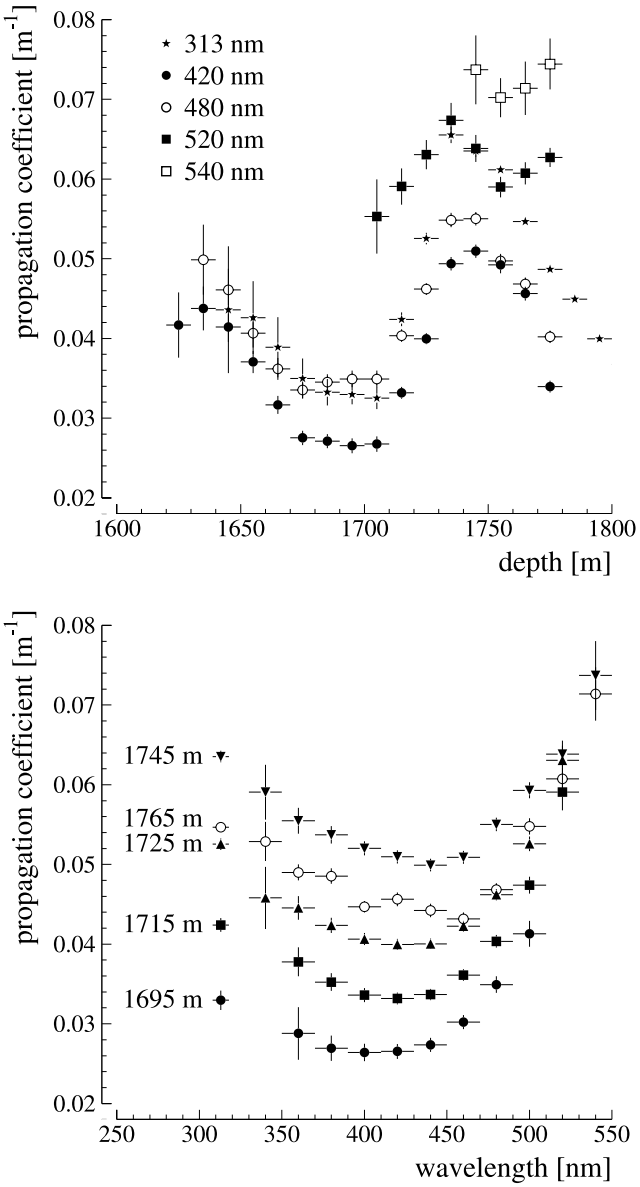

Figure 12. Propagation coefficient c_p extracted from fluence fits to steady source data for selected (top) wavelengths and (bottom) depths. The depth dependence exhibited the same dust-correlated variations as the pulsed data (Figure 10), with a dust peak at ~1740 m and the onset of a shallower peak. In agreement with the three-component model of absorptivity, equation (8), the wavelength dependence had a minimum where a falling power law due to absorption by dust was comparable to a rising exponential due to intrinsic ice absorption.

in Figure 13. Included in Figure 13 are measurements made at depths between 800 and 1000 m [*Askebjer et al.*, 1997b]. Because at these depths scattering is dominated by air bubbles trapped in the ice and therefore does not depend on wavelength, the data points between 800 and 1000 m are averages over measurements between 410 and 610 nm. The scattering coefficient falls off monotonically with depth down to ~1400 m. This is consistent with the prediction that bubbles compress and eventually convert to nonscattering air hydrate crystals. At depths greater than 1400 m, we identify a structure of four distinct peaks (labeled A, B, C, D), which have previously [*Price et al.*, 2000] been correlated to peaks in dust concentration due to stadials during the last glacial period in the late Pleistocene which have been measured in ice cores. Peak D corresponds to an age of ~65,000 years. On the basis of peak matching with ice core data, we expect a strong dust peak due to the Last Glacial Maximum at a depth of approximately 1300 m. However, in this region our scattering data may still be dominated by bubbles and the LGM peak is either hidden under the bubble scattering or smoothly transitions to it in the data. From our scattering data alone we cannot determine to what extent the increased dust concentration at the LGM contributes to scattering from bubbles.

[44] In the most densely instrumented depth range, between ~1530 and 2000 m, we measured scattering for at least two (and up to four) wavelengths and could therefore fit the wavelength dependence. A power law, $b_e(\lambda) \propto \lambda^{-\alpha}$, was fitted in all depth bins simultaneously (Figure 14), yielding $\alpha = 0.90 \pm 0.03$, where the error includes a 5% systematic uncertainty that was added in quadrature to the statistical error of each data point (see section 6 for a discussion of systematic uncertainties). The χ^2 for the fit was 120.8 for 129 degrees of freedom (130 data points and one fitted parameter), corresponding to a 68% probability.

[45] To investigate a possible depth dependence of α due to varying dust composition, we performed separate power law fits in individual depth bins. The results are shown in Figure 15 (top). Figure 15 (bottom) compares ratios of fitted scattering coefficients b_e for all wavelength combinations with the ratios from the global power law fit. The depth dependence of the fitted power law exponent is flat in the region between 1780 and 1860 m where we had data at all four wavelengths. Outside this range, the fluctuations in α closely follow the ratio between $b_e(370)$ and $b_e(532)$, with some features also seen in the $b_e(470)/b_e(532)$ data. However, the structure was not reproduced in the $b_e(370)/b_e(470)$ ratio. We used the dust structure seen in the scattering data (Figure 13) as a template for dust-induced variations with depth, and fitted it to the depth dependence of α through linear scaling. A fit of the template to the entire 1500–2000 m range yielded a profile that was consistent with a constant α (see nearly flat curve with light gray one-standard-deviation error band in Figure 15). When the same 500-m template was fitted only to the data between 1650 and 1800 m, where α seemed to follow the dust structure, the resulting curve poorly described the data outside the range included in the fit. We concluded that the fluctuations in α were caused by statistical fluctuations in the measured scattering coefficients and minor unresolved systematics in measurements of $b_e(532)$. The standard deviation in the distribution of fitted α constants was consistent with this conclusion and hence with the fact that a depth dependence in the wavelength dependence of scattering was beyond the sensitivity of our measurements.

5.2. Absorption

[46] Absorptivity measured with pulsed data (Figure 16) is much stronger at 532 nm than at the shorter wavelengths, in agreement with the three-component model. A broad peak due to the LGM is visible around 1300 m, mainly at

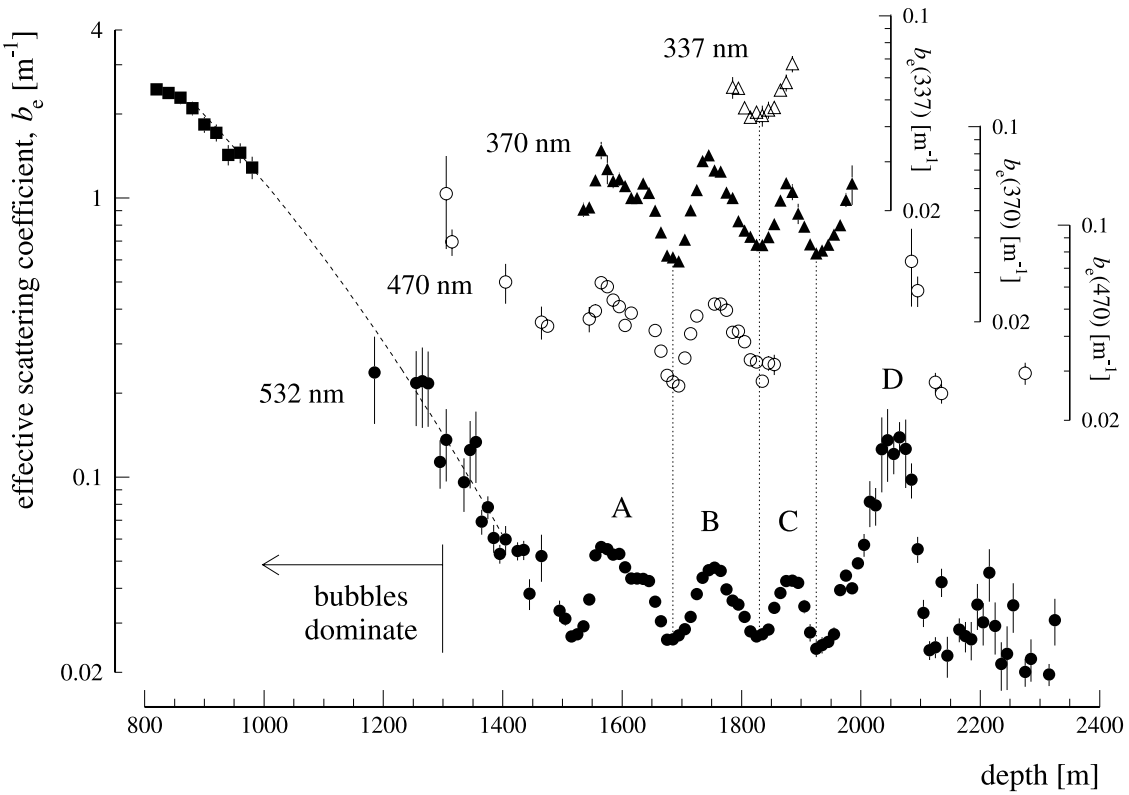

Figure 13. Depth dependence of the effective scattering coefficient measured with pulsed sources at four wavelengths. Data at 337, 370, and 470 nm are rescaled for clarity according to the axes to the right. The four peaks labeled A through D correspond to stadials in the last glacial period. A broad dust peak due to the Last Glacial Maximum, expected at ~1300 m, is masked by bubble scattering. The points between 800 and 1000 m, where scattering is dominated by bubbles and does not depend on wavelength, are weighted means of previously published measurements at 410–610 nm [*Askebjer et al.*, 1997b].

532 nm but also in the 470 nm data. The smaller dust peaks (A, B, C) are seen at the shorter wavelengths, and the 470 nm data are also consistent with the larger peak D, but this dust structure is largely suppressed in the 532 nm data because of the relative strength of intrinsic molecular absorption by the ice at this wavelength. The LGM is visible in absorption despite the bubbles, since bubbles do not absorb, only scatter light. Since the ice component dominates for the longest wavelength, we can see a weak slope of $a(532)$ with depth that goes beyond the small variations due to dust. *Woschnagg and Price* [2001] found that this is due to a temperature dependence of the molecular absorption which amounts to an increase in $a(532)$ of 1% per degree K. For the shorter wavelengths, ice absorption is negligible compared with dust absorption and the temperature effect is not detectable.

[47] In addition to the direct measurements of absorption with pulsed data, absorptivity was also extracted from a combination of steady and pulsed data. An inversion of equation (20),

$$a = \frac{c_p^2}{3b_e}, \tag{22}$$

suggested a way to calculate the absorption coefficient by combining the scattering coefficient (Figure 13) with the propagation coefficient (Figure 12). At each wavelength where we had measured the propagation coefficient c_p, the depth profile of b_e was calculated from pulsed data by averaging over the (up to) four available wavelengths after translating to the appropriate wavelength with the measured $\lambda^{-0.9}$ power law. The absorption coefficient at this wavelength was then calculated with equation (22). This procedure resulted in depth profiles of $a(\lambda)$ at 13 wavelengths between 313 nm (from UVM data) and 560 nm (from RM data). For each depth bin, the available measurements of absorptivity (the direct measurements at up to four wavelengths from pulsed data and the inferred measurements from steady data) were then combined. A two-component model of absorption (disregarding the Urbach component which is negligible at wavelengths greater than 300 nm) of the form

$$a(z) = C_{\text{dust}}(z)\lambda^{-\kappa} + A_{\text{IR}}e^{-\lambda_0/\lambda} \tag{23}$$

was fitted simultaneously to all depth bins z_i which contained at least five data points, keeping A_{IR}, λ_0, and κ the same for all bins and allowing only the dust concentration parameter C_{dust} to vary with depth. In this global fit, the ice exponential in the infrared was corrected for the 1%/K temperature dependence that *Woschnagg and Price* [2001] measured at 532 nm and that was assumed to

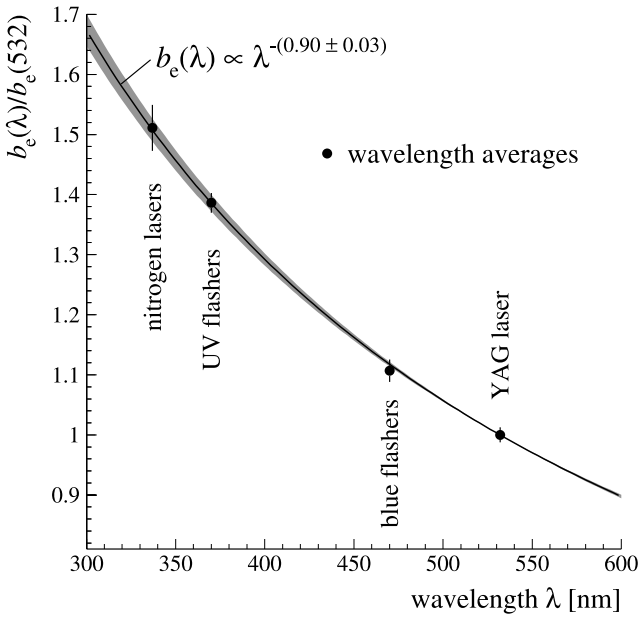

Figure 14. Wavelength dependence of scattering. A power law $\lambda^{-\alpha}$ with $\alpha = 0.90 \pm 0.03$ was fitted to the effective scattering coefficients $b_e(\lambda)$ measured with pulsed data at four wavelengths. The data points are wavelength averages (normalized with $b_e(532)$) and the shaded curve covers the one-standard-deviation uncertainty (including systematics) in the fitted power law.

be valid over the entire wavelength range. This correction was normalized to zero at a depth of 1730 m, the location of the array center. At 1600 m the ice is 2.4 K colder than at 1730 m, and at 1900 m it is 3.4 K warmer [*Price et al.*, 2002].

[48] Figure 17 illustrates the two-component fits in 20 depth bins between 1600 and 1800 m, showing both steady and pulsed data together with the fitted model and its two components. The errors shown (and used for the fit) are a combination of the statistical errors and a 5% systematic uncertainty on every data point (see section 6 for a discussion of systematics). Between 1800 and 1900 m, only pulsed measurements were available. In this range we kept κ fixed at the value from the fits at 1600–1800 m, and fitted only the dust concentration parameter to pulsed data. The χ^2 of the combined fit in all 30 depth bins between 1600 and 1900 m was 247.3 for 239 degrees of freedom, corresponding to a 34% probability, confirming that the two-component model described the data well, within the estimated uncertainties. The agreement between the pulsed data points and the steady data points in Figure 17 is further evidence that the results are valid within the quoted errors. The exponent of the power law wavelength dependence for dust absorption was $\kappa = 1.08 \pm 0.01$. Fitting the exponential due to intrinsic absorption by ice exclusively with absorption data from this analysis yielded $A_{IR} = (6954 \pm 973)\ m^{-1}$ and $\lambda_0 = (6618 \pm 71)$ nm. For comparison, a previous fit of this component to laboratory ice data from *Grenfell and Perovich* [1981] (shown in Figure 19) yielded the parameters $A_{IR} = 8100\ m^{-1}$ and $\lambda_0 = 6700$ nm [*Askebjer et al.*, 1997a], in excellent agreement with our results based on in situ ice data. The fit to the laboratory data was limited to the spectral range 600–800 nm to avoid the data at the less absorbing wavelengths which contained a large scattering component.

[49] The depth dependence of the fitted dust concentration parameter C_{dust} (Figure 18) tracks the profile caused by dust layers seen in pulsed scattering data and in absorption

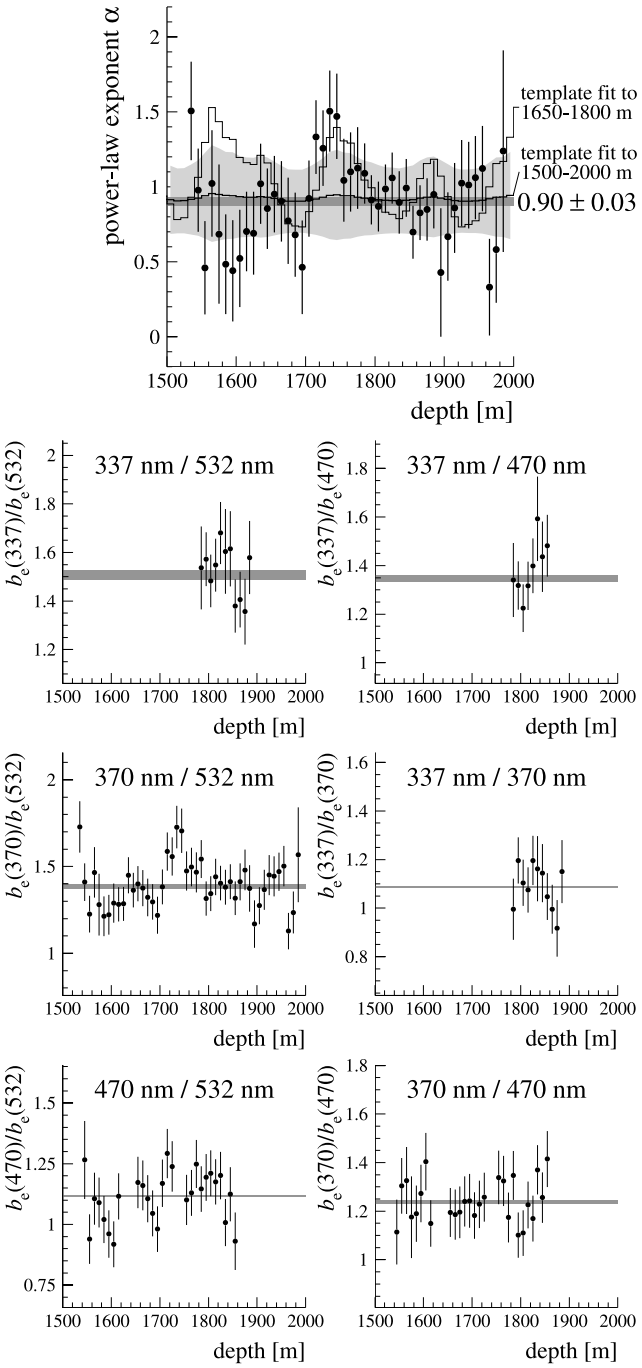

Figure 15. (top) Depth dependence of the power law exponent α fitted to the wavelength dependence of scattering and (bottom) ratios of b_e for different wavelength combinations. Averages from the global fit (Figure 14) are shown as shaded lines with one-standard-deviation widths. A template for depth-dependent variations following the dust structure seen in scattering data (Figure 13) was used to evaluate the correlation of α with dust concentration.

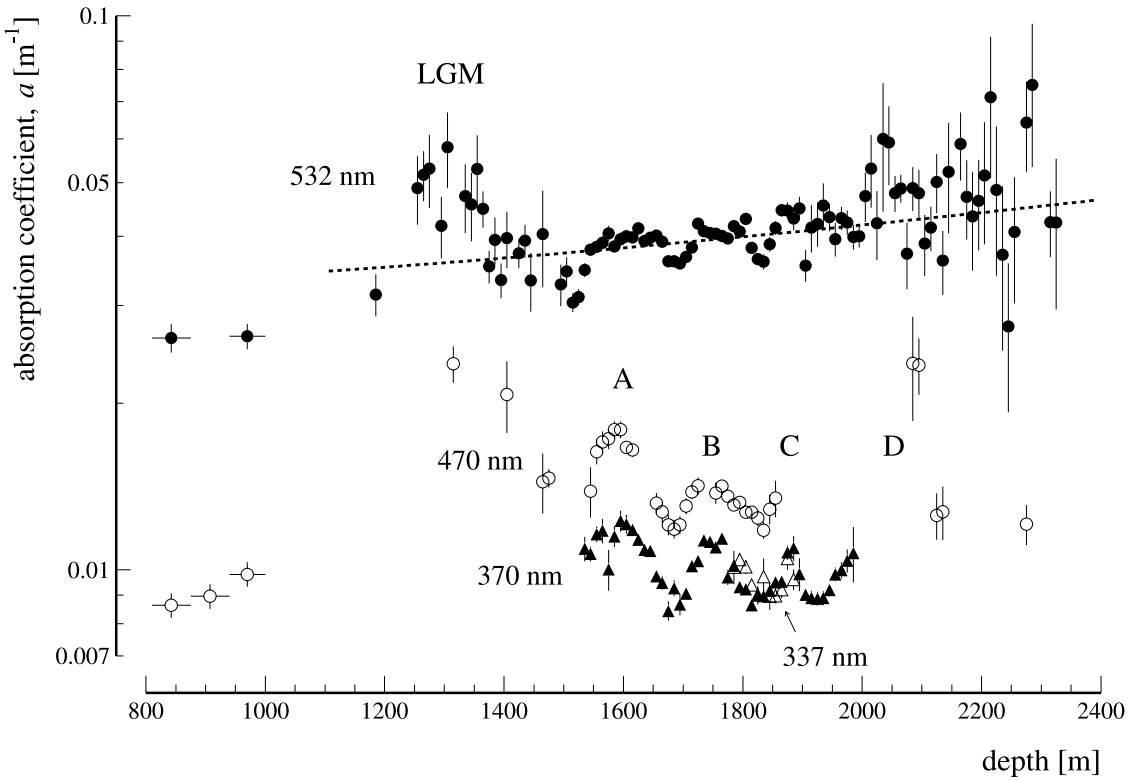

Figure 16. Depth dependence of absorptivity measured with pulsed sources at four wavelengths. At 532 nm the ice component dominates and is superimposed on smaller variations due to dust. The dashed line outlines a 1%/K increase in ice absorptivity with temperature. The broad peak at ~1300 m is due to the LGM. At the shorter wavelengths, the dust peaks A, B, and C are clearly seen, and at 470 nm the data are consistent with the relatively stronger peak D and with clearer ice below this peak. The points between 800 and 1000 m are from measurements with an AMANDA precursor detector [*Askebjer et al.*, 1997b].

for wavelengths shorter than ~500 nm where dust dominates over ice. The scattering profile at 400 nm was calculated by averaging the measured depth profiles at four wavelengths (Figure 13), interpolated to 400 nm via the power law wavelength dependence. Within our experimental uncertainties, the correlation between C_{dust} and $b_e(400)$ is linear in the range covered by our measurements (see fit in Figure 18 (bottom)), supporting the premise of the three-component model that absorptivity caused by dust (which is stronger than intrinsic ice absorption for wavelengths between ~200 and ~500 nm) is proportional to dust concentration and has a power law wavelength dependence.

[50] We investigated the depth dependence of κ by attempting a two-component fit to the same absorption data (Figure 17), while fixing the infrared exponential with the values obtained from the fit that assumed a constant κ (discussed above) and allowing both C_{dust} and κ to vary with depth. However, in many of the depth bins the data did not extend low enough in wavelength (<400 nm), and did not have sufficiently small errors, to give stable fits of both κ and C_{dust}, given that they are highly correlated. We concluded that, within the sensitivity of our absorption measurements, there was no evidence of a depth dependence for κ. This was supported by our Mie calculations of absorptivity due to dust (and those by *He and Price* [1998]), which showed only a weak dependence of κ on dust grain size.

[51] In Figure 19, we compare our measurements of absorptivity in South Pole ice at three depths greater than 1500 m with measurements between 800 and 1000 m [*Askebjer et al.*, 1997a], and with measurements of absorptivity on laboratory-grown ice, as reviewed by *Warren* [1984]. In South Pole ice, depths greater than 1500 m correspond to ages in the late Pleistocene and depths between 800 and 1000 m correspond to the onset of the relatively warmer Holocene time period after the Last Glacial Maximum. During the Holocene, dust concentrations in the atmosphere were significantly lower than during earlier periods. The dust flux ratio between the LGM and the Holocene measured in an ice core from Dome C (East Antarctica) is ~26 [*Delmonte et al.*, 2002]. The laboratory measurements in the range 400–1400 nm are by *Grenfell and Perovich* [1981], and those between 250 and 400 nm are by *Perovich and Govoni* [1991]. At longer wavelengths, ice absorptivity displays spectral structure corresponding to modes of molecular stretching and bending. The rising exponential from our fit to glacial ice data closely tracks the exponential increase in the laboratory data longward of 600 nm, approximating the average in this range. The measurements at the Urbach tail in the far UV were made by *Minton* [1971].

6. Systematic Uncertainties

[52] We considered a number of potential systematic error sources that could have affected our measurements of optical parameters, and investigated their impact on our

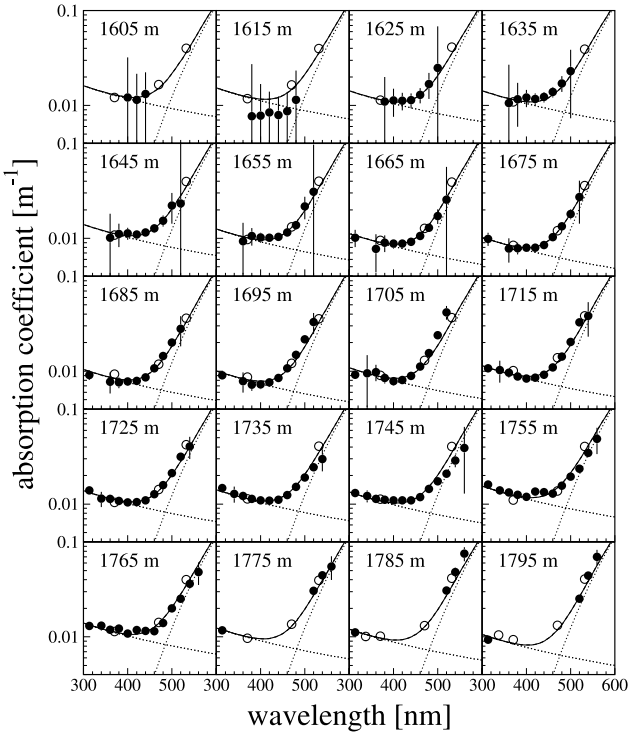

Figure 17. Wavelength dependence of absorption. The solid curves show the two-component model fitted simultaneously to pulsed data (open circles) and steady data (solid circles) in twenty 10 m depth bins. The dotted curves show the two components: a sharply rising exponential, identical for all bins, due to intrinsic ice absorption, and a slowly falling power law that describes absorption due to dust. The power law exponent κ is the same in all bins, but the normalization C_{dust} depends on depth (see Figure 18). The error bars include a 5% systematic uncertainty. Errors on data points from steady data decrease with increasing depth, as statistics improve when receivers are closer to the emitters located at ~1850 m.

results. Our estimates of systematic errors are summarized in Table 2.

6.1. Systematics in Timing Measurements

[53] For the simulation-based fits to photon timing data, the effects of systematics were estimated by varying our modeling of associated physical processes and detector characteristics in the photon propagation simulation within ranges that reflected the uncertainty in our knowledge.

[54] The mean scattering angle was varied in the simulations to allow for uncertainties in our modeling of dust. We varied $\langle \cos\theta \rangle$ in steps of 0.1 between 0.4 and 0.99, extreme values bracketing (but well outside) a realistic range, and generated full samples of simulated time distributions for each value of $\langle \cos\theta \rangle$. The entire 370 nm data set, which covered most of the studied depth range and was sensitive to both scattering and absorption by dust, was then reanalyzed with each $\langle \cos\theta \rangle$ sample in turn (the effect would be similar for the other data samples). We found a weak dependence of the fitted values of λ_e and λ_a on the choice of $\langle \cos\theta \rangle$: both parameters decreased linearly by ~2.5% for each increase of 0.1 in $\langle \cos\theta \rangle$.

[55] The importance of the emitted spatial light distributions was investigated by repeating all fits to pulsed data with three different emission pattern descriptions in the Monte Carlo simulation: isotropic, vertically peaked cos θ, and 45° tilted cos θ. The actual emission pattern was well known for the YAG laser and the nitrogen lasers, with some distortions due to the glass spheres expected for the emission patterns from the LED sources. The differences be-

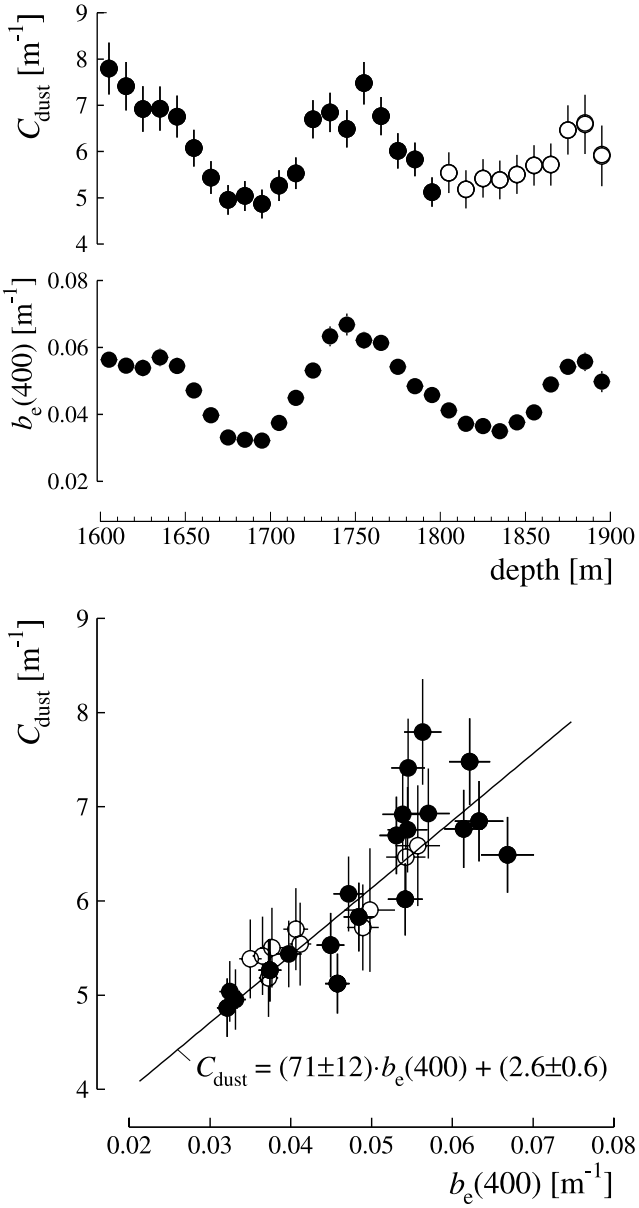

Figure 18. Correlation between scattering and absorption due to dust. (top) Comparison of the depth dependences of the dust concentration parameter C_{dust} in the two-component model of absorptivity and the effective scattering coefficient at 400 nm. (bottom) A linear fit to their correlation. The solid circles indicate values of C_{dust} from fits to both pulsed and steady data (Figure 17), and the open circles indicate values from fits to pulsed data only.

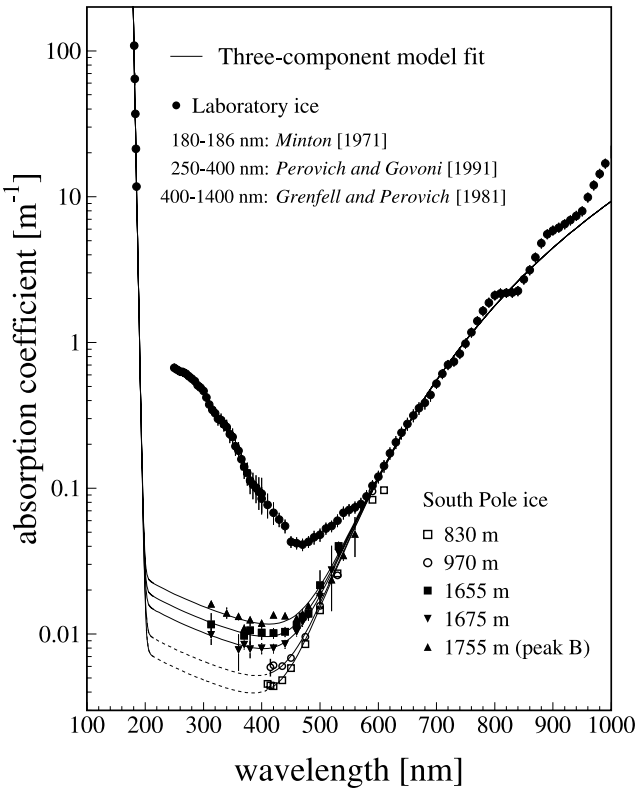

Figure 19. Wavelength dependence of absorption from ultraviolet to infrared, for deep South Pole ice and for laboratory-grown ice (from a compilation by *Warren* [1984]). Results from the present work are shown for three depths. South Pole data between 800 and 1000 m are from *Askebjer et al.* [1997a].

tween the three simulated source shapes overestimated the uncertainties due to distortions by the glass. Even so, the effect on the fitted parameters was only 1–2% for λ_e and <1% for λ_a.

[56] The optical properties of the refrozen columns of ice around the strings (~30 cm in radius) differ from those of the bulk ice, mainly owing to a higher concentration of air bubbles trapped in the ice near the modules which have not had time to convert to nonscattering air hydrate crystals, and to a lesser degree because of impurities introduced during drilling. This mainly affects the angular acceptance of the optical modules by making it slightly more isotropic, scattering downward traveling photons into, and upward traveling photons away from, the PMT photocathode plane. We repeated all fits to pulsed data with simulated samples generated with different models of angular OM efficiency, based on calibration measurements in the laboratory and in situ, and found that the results were quite insensitive to a wide range of realistic OM acceptance models. Using our simplified acceptance model, the uncertainty in the measured coefficients was estimated to be 1–2%.

[57] Uncertainties related to basic detector calibrations (array geometry and photon hit timing) affected the timing fits by convoluting Gaussian errors with the delay time distributions. The relative positions of optical modules and light sources were known to less than 1 m, which translated to an uncertainty in timing of less than 5 ns. The timing calibration yielded an uncertainty in individual relative hit times of 5 ns, the same order as the uncertainty in the array geometry. The impact of these uncertainties on the fitted optical properties was investigated by randomly smearing hit times in the simulated time distributions by 5 and 10 ns. The effect was found to be small: less than 1% for both scattering and absorption. An additional uncertainty lies in the timing of the start of the pulse, which was first estimated from pulses in the OM nearest to the source and then fitted as an offset. However, the effect on the measured parameters was negligible.

[58] In the analysis of pulsed data, the sources were assumed to be monochromatic and no wavelength dependence was applied to the simulation. Only the LED flasher sources had a considerable spread in their wavelength spectrum (Table 1), which was relatively symmetric around a well-defined mean. Since both scattering coefficient (Figure 14) and absorptivity (Figure 17) vary smoothly with wavelength, the spectral spread translated to a spread in the distribution of fitted optical parameters in each depth bin, creating a larger variance, but not significantly affecting the averages or their errors. By folding in the LED wavelength spectra with the measured wavelength dependences, we estimated the overall effect on the fitted parameters at 370 and 470 nm to be less than 1%. The effect on the power law exponent α for scattering and on the parameters of the two-component description of absorptivity were considerably smaller than the statistical errors.

[59] In the Monte Carlo simulation, the temporal distribution of photons emitted in the light pulses from a specific source was modeled closely to the measured curve, which for all pulsed sources was estimated to be accurate to within a few nanoseconds. Varying the pulse width by this uncertainty affected the measured parameters less than an uncertainty of the same magnitude in the photon timing, since at short distances only the first of several photons was used

Table 2. Estimates of Systematic Uncertainty in Measurements of Scattering (b_e), Absorption (a), and Propagation (c_p) Coefficients

	Timing Fits		Fluence Fits	
Systematic Error Source	σ_{b_e}	σ_a	σ_{c_p}	σ_a[a]
Light propagation modeling				
Mean scattering angle $\langle\cos\theta\rangle$	2.5%	2.5%	—	2.5%
Velocity of light in ice	<0.5%	<0.5%	—	<0.5%
Light source characteristics				
Spatial emission pattern	<2%	<1%	<0.5%	<2%
Emission time profile	<1%	<1%	—	<1%
Wavelength spectrum	<1%	<1%	<1%	<1%
Detector calibrations				
Time resolution	<1%	<1%	—	<1%
Geometry calibration	<1%	<1%	<1%	<1%
Properties of refrozen ice column	<2%	<2%	—	<2%
Absolute OM detection efficiency	—	—	—	—
Relative OM detection efficiencies	—	—	<1%	<1%
Methodology				
Time distribution binning	<0.5%	<0.5%	—	<0.5%
Averaging over depth[b]	<2%	<2%	<2%	<2%
Total systematic error	5%	5%	3%	5%

[a]Combination of error in b_e from timing measurements and error in c_p from fluence analysis.

[b]Effect estimated from overall agreement between c_p from the two analysis techniques.

and at larger distances statistical uncertainties in scattering dominated.

[60] The velocity of light is determined by the group velocity refractive index of ice, n_g, which decreases monotonically with increasing wavelength, from 1.38 at 337 nm to 1.33 at 532 nm [*Price and Woschnagg*, 2001]. We used the known wavelength dependence in our simulations and generated time distributions for sources at given wavelengths with the corresponding refractive indices. The uncertainties in n_g were small, and the uncertainties in the fitted parameters were negligible.

[61] The sensitivity to the binning of the time distributions was studied by repeating all fits with the data binned in 2, 5, and 20 ns-wide bins in addition to the nominal 10 ns binning. No systematic effects were found and the fit results for the four bin sizes agreed within the statistical uncertainties.

[62] A potential systematic error comes from integrating over varying ice properties by sampling photons that have traveled through several ice layers, even when emitter and receiver were in the same horizontal layer. However, a comparison with results from fluence analyses which measured optical properties more locally (see section 6.3 for a discussion) showed that no significant smoothing of depth-dependent variations had occurred in our pulsed measurements, within the ~10 m depth resolution.

[63] On the basis of these investigations into potential error sources, we assigned a 5% overall systematic error to the optical parameters (averaged in 10 m depth bins) from fits to pulsed data.

6.2. Systematics in Fluence Measurements

[64] Most of the main systematic error sources in the timing measurements did not affect the fluence analysis of steady source data, since the latter did not depend on a detailed simulation of photon propagation and detection. Systematics in measurements of the propagation coefficient c_p were therefore smaller than systematics in measurements of b_e and a with pulsed data, and for absorptivity measured with a combination of both data sets the systematics were dominated by the 5% systematic uncertainty in b_e.

[65] The wavelength spectra of the steady sources were symmetric around the nominal wavelengths and had widths comparable to those of the pulsed LED sources. From the smooth wavelength dependences of absorption and scattering, the systematic uncertainty in c_p was estimated to be less than 1%. We also varied the wavelengths for the absorptivity points from steady data in the global two-component fit (Figure 17) by one standard deviation (5 nm for the UVM and 10 nm for the RM). The effect on the fitted parameters κ and C_{dust} was smaller than their statistical uncertainties.

[66] A systematic shift of 1 m in the relative positions of emitters and receivers translates to a shift of less than 1% in individual measured c_p, since most distances used in the analysis were greater than 100 m. Since uncertainties in the geometry calibration were distributed symmetrically around the mean, these errors made the variance in each depth bin correspondingly larger, but affected the average and its error only marginally.

[67] The fluence analysis was not sensitive to an uncertainty in the absolute OM detection efficiency, ϵ, since a global normalization factor cancels out in calculations of the propagation coefficient with equation (21). Variations in the relative efficiencies between optical modules, $\epsilon_A \neq \epsilon_B$, correlate directly with the relative error in c_p,

$$\frac{\sigma_{c_p}}{c_p} \approx \left|\frac{\epsilon_B}{\epsilon_A}\right|, \tag{24}$$

given that $\langle c_p \rangle \approx 0.04$ and $\langle \Delta d \rangle \approx 20$ m. However, since such variations were distributed around a mean, the systematic effect on our results was negligible. Within each 10 m depth bin, the variance of the distribution of fitted parameters was sensitive to relative detection efficiencies, but the average and its error were not significantly affected.

[68] The effect of the steady source light emission patterns on the fluence analysis was investigated with Monte Carlo simulations and found to be negligible at the distances used in the analysis.

[69] The overall systematic uncertainty in the fitted propagation coefficients, averaged in 10 m depth bins, was estimated to be a few percent. For the wavelength-dependent absorptivity measurements, made with a combination of pulsed data and steady data, we assigned a slightly larger systematic uncertainty of 5%, stemming from the pulsed measurements of scattering coefficient.

6.3. Consistency Checks

[70] By combining methods and results of the two independent techniques (simulation-based fits to photon timing data from pulsed light sources and fluence fits to steady source data) we could estimate the overall systematic uncertainties of both methods. For this purpose, we analyzed the pulsed source data with the same fluence method that was applied to the steady source data, by using receiver count rates instead of timing information. For each event (i.e., each light pulse from the source) the number of recorded pulses (hits) was calculated for every receiver. The time-to-digital converters in the data acquisition electronics could record up to eight hits in each triggered event. For receivers with eight recorded hits in any event in a run, data were discarded from the analysis of the run since the fraction of unrecorded photons was not known. This counting procedure resulted in total count rates for all receivers that were not saturated in the run. These data were then used for the same fluence analysis as the steady data and propagation coefficients c_p were calculated with equation (21). As a consistency check, we also estimated the count rates from the mean number of photoelectrons, $\langle N_{pe} \rangle$, recorded by each receiver. The two counting methods gave the same results within the statistical uncertainty. Figure 20 shows a comparison between the propagation coefficients obtained with fluence analyses of flasher data at 370 and 470 nm and the corresponding $c_p = \sqrt{3ab_e}$, where a and b_e were determined with timing fits to the same data. Furthermore, since the wavelengths of these two sources fell in the range covered by the Rainbow Module, we could also compare the propagation coefficient extracted from steady source data at the same wavelength. For a comparison with 370 nm data and 470 nm data, the average c_p for 360 and 380 nm, and for 460 and 480 nm, respectively, are included in Figure 20. The results from the three analyses on two sets of data largely agree within the statistical errors plus a systematic uncertainty of 5%, with some slightly larger

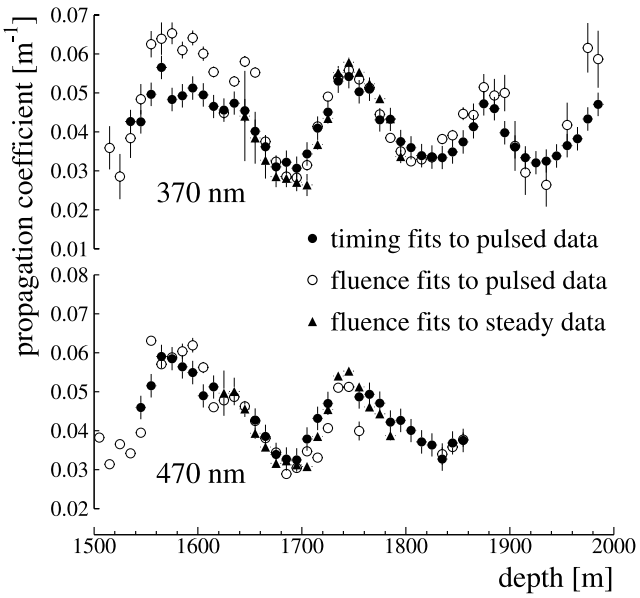

Figure 20. Comparison of propagation coefficient c_p at 370 and 470 nm measured with three methods: a fluence analysis of steady source data (triangles); photon timing fits to pulsed data (solid circles); and a fluence analysis of pulsed data (open circles). The error bars show only the statistical uncertainties.

disagreements due to unresolved systematics. The overall agreement lends confidence to both methods and sets an upper bound on systematic uncertainties in agreement with our estimates in this section.

[71] There were three important differences between the fits to time-of-flight information from pulsed data and fluence fits to steady data which made them complementary and which we used for cross checks. First, with the timing data we could distinguish between scattering (b_e) and absorption (a); from the steady data we could only extract the product as expressed in the propagation coefficient (c_p). Second, the timing fits were based on Monte Carlo simulations, which required knowledge and assumptions about detector and medium characteristics and about the mechanics of photon propagation, and which were sensitive to uncertainties related to calibrations. The fluence fits were model-independent and only required data to be collected in the diffusive regime. The third difference was that the timing fits probed all ice between emitter and receiver and hence data had to be recorded within relatively homogenous regions of ice. Timing fits thus did not work well for light propagation through regions with varying optical properties, where the resulting depth profile tended to suffer some smearing through averaging over depths. In contrast, steady source data probed local ice by comparing light fluxes at nearby pairs of receivers. Hence pulsed data probed the ice horizontally and steady data probed vertically.

7. Discussion

[72] We now have a detailed understanding of what causes absorption and scattering in glacial ice at the South Pole. Measurements presented in this paper map the full wavelength dependence of scattering and absorption in South Pole ice for visible light to the ultraviolet. The power law dependences for both scattering and absorption by dust predicted by Mie theory calculations were confirmed, and the power law indices for the particular dust composition were determined for both cases. The exponent for scattering is -0.90 ± 0.03, and the exponent for absorption is -1.08 ± 0.01, where the errors include a 5% systematic uncertainty on individual data points used to fit the power laws. The optical transparency of pure ice free of impurities for UV to visible wavelengths is still an open question. Solid state theory does not offer guidance as to absorptivity of dust-free ice, but it must be very low.

[73] The depth-dependent optical properties of ice at the South Pole are crucial for operation of the IceCube neutrino observatory [*Ahrens et al.*, 2004a], for the AMANDA detector embedded in IceCube, and for analysis of optical signatures of neutrinos from potential astrophysical sources. A detailed description of scattering and absorption is needed to accurately simulate Cherenkov photon propagation through ice and to predict photon arrival times and amplitudes recorded by the photomultiplier tubes in the arrays. Such simulations form the basis for detector simulations and for reconstruction of event topologies induced by secondary charged leptons created in neutrino interactions near the detector [*Ahrens et al.*, 2004b]. The accuracy to which trajectories and energies of neutrinos can be determined depends on how realistically light propagation is modeled. The λ^{-2} wavelength spectrum of Cherenkov light, when convolved with the glass transmission characteristics and the PMT quantum efficiency, results in an optical module sensitivity maximum near 400 nm, where, incidentally, the ice is most transparent.

[74] At depths between 1100 and 1500 m, our measurements of optical properties are predominantly at 532 nm, with a few data points at 470 nm. Scattering data at shallow depths are dominated by scattering off air bubbles, which overshadows any underlying dust structure (Figure 13) such as the large increase in dust concentration due to the Last Glacial Maximum. At the longer wavelength, absorptivity is dominated by intrinsic ice absorption, which masks most of the dust structure, thus revealing a weak depth dependence due to temperature variations. However, LGM dust concentrations are sufficiently high to cause a broad peak in absorptivity to emerge around 1300 m (Figure 16), a peak also visible in the 470 nm data. Nevertheless, the absorption data for depths less than $\sim$1500 m are too sparse to allow us to fully track dust absorptivity up to 1100 m.

[75] In Figure 21, we compare our measurements of scattering and absorption with dust concentrations measured in Antarctic ice cores. The optical parameters measured with pulsed data at different wavelengths were interpolated to 400 nm, using the fitted power laws, and averaged. For scattering, data at all four available wavelengths were used, but for absorption the 532 nm data were excluded since they were only weakly sensitive to dust. The smoothed curve in Figure 21 (left) is derived from a 50-m running average of dust mass concentrations measured in ice cores from Vostok [*Petit et al.*, 1999] and Dome Fuji [*Watanabe et al.*, 1999]. Both stations are $\sim 10^3$ km from the South Pole on ice with different age versus depth relationships. A South Pole depth chronology, previously determined through peak matching

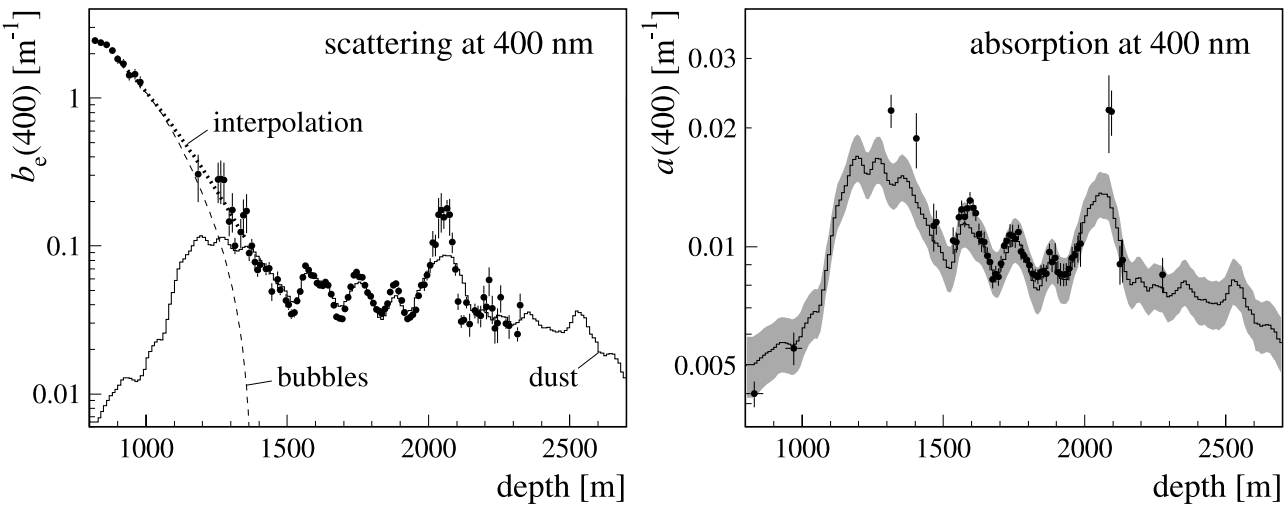

Figure 21. Correlation of dust concentration with (left) scattering and (right) absorption at 400 nm. The dust profile in Figure 21 (left) is derived from a 50-m running average of dust mass concentration measured in ice cores from Vostok [*Petit et al.*, 1999] and Dome Fuji [*Watanabe et al.*, 1999] and translated to South Pole depths. It has been linearly scaled to match the data points between 1600 and 1900 m. The dashed line is an estimate of the contribution to scattering by bubbles. The shaded band in Figure 21 (right) contains the one-standard-deviation estimate of absorptivity calculated by applying the linear correlation in Figure 18 to the dust contribution to scattering in Figure 21 (left).

of ice core dust data with peaks A through D seen in preliminary AMANDA data [*Price et al.*, 2000], was used to extrapolate the core dust concentrations to South Pole depths. Between 1500 and 2000 m, the agreement along the depth scale is therefore by design. Mass concentrations were raised to the power 2/3 (explained at the end of this section), and the resulting profile was scaled linearly to fit our scattering measurements between 1600 and 1900 m. On the basis of a comparison of the dust profile at depths less than 1500 m with our scattering data, we estimated the topology of the decrease in bubble scattering. We first interpolated the scattering coefficient between the measurements presented in this work and measurements in shallower ice by *Askebjer et al.* [1997a], and then subtracted the contribution from dust scattering assumed to follow the dust profile. The resulting contribution to scattering by bubbles (the dashed line in Figure 21) becomes vanishingly small at $\sim$1350 m.

[76] We used the dust profile in Figure 21 (left) as an estimate of $b_e(400)$ due to dust, and applied the fitted correlation between $b_e(400)$ and C_{dust} (Figure 18) along with equation (23) to estimate absorptivity at 400 nm. The resulting depth dependence of $a(400)$ is shown in Figure 21 (right) together with our measurements. The shaded band indicates the one-standard-deviation uncertainty due to statistical errors in the parameters used in the calculation. Absorption data at depths between 800 and 1000 m by *Askebjer et al.* [1997b] are in agreement with our extrapolated estimate, and track the decrease in dust concentration after the Last Glacial Maximum. In the regions with highest dust concentration, peak D and at the LGM, the dust extrapolation underestimates absorptivity (at peak D, scattering is also underestimated). This could be partly explained by the low depth resolution in the ice core data, and, to a lesser extent, our averaging procedure which suppressed large variations over depth scales smaller than 50 m.

[77] In scaling dust mass concentrations from Vostok and Dome Fuji ice cores to our measurements of scattering and absorption, the power 2/3 converts from volume to scattering cross section in the limiting case of constant particle number density. Using a power closer to 1, corresponding to the limiting case of constant particle sizes, causes the extrapolation to overestimate absorptivity at the data points between 800 and 1000 m by up to 50%, whereas between 1100 and 2600 m it yields the same results (within 10%) as when scaling with the power 2/3. Since the purpose of the comparison with ice core dust concentration (Figure 21) was to interpolate between our data points, we chose the scaling which gave the better empirical fit to our absorption data. In reality, particle size does increase with dust mass concentration [*Ruth et al.*, 2003], so the true scaling is likely a power between 2/3 and 1.

8. Conclusion

[78] On the basis of the measurements presented in this paper, we developed a model with six parameters to describe the optical properties of South Pole ice throughout the wavelength range 300–600 nm and for depths in the interval 800–2700 m. In this model, we use the depth dependences at 400 nm of the effective scattering coefficient, $b_e(400)$, and the dust absorptivity, $a_{dust}(400) = C_{dust} \cdot (400)^{-\kappa}$, as starting points. Values of $b_e(400)$ and $a_{dust}(400)$ for every 10 m in depth are listed in Table 3. The dust profiles in Figure 21 were used for extrapolation to depths where we did not have data, except for $b_e(400)$ at depths less than 1350 m where we used an interpolation between data from the shallow and the deep AMANDA detectors (see dotted line in Figure 21 (left)). Two parameters (see values in Figure 18), determined with the linear fit to the

Table 3. Effective Scattering Coefficient (b_e) and Dust Absorptivity (a_{dust}) at 400 nm Versus Depth in the Ice at the South Pole[a]

Depth, m	$b_e(400)$, $10^{-2}m^{-1}$	$a_{dust}(400)$, $10^{-3}m^{-1}$	Depth, m	$b_e(400)$, $10^{-2}m^{-1}$	$a_{dust}(400)$, $10^{-3}m^{-1}$	Depth, m	$b_e(400)$, $10^{-2}m^{-1}$	$a_{dust}(400)$, $10^{-3}m^{-1}$
805	(276)[b]	[4.6][c]	1455	(5.5)	(9.8)	2105	4.2 ± 0.5	8.4 ± 1.3
815	(265)	[4.6]	1465	6.0 ± 0.8	10.3 ± 1.6	2115	3.1 ± 0.3	7.2 ± 1.1
825	*245 ± 41*[d]	[4.6]	1475	5.0 ± 0.4	9.3 ± 1.3	2125	3.2 ± 0.2	7.3 ± 1.1
835	(244)	[4.6]	1485	(4.7)	(8.9)	2135	4.2 ± 0.4	8.4 ± 1.2
845	*238 ± 40*	[4.7]	1495	4.3 ± 0.4	8.5 ± 1.3	2145	3.0 ± 0.5	7.1 ± 1.2
855	(224)	[4.8]	1505	4.0 ± 0.3	8.2 ± 1.2	2155	(3.3)	(7.5)
865	*228 ± 39*	[4.9]	1515	3.5 ± 0.2	7.6 ± 1.1	2165	3.7 ± 0.4	7.8 ± 1.2
875	(205)	[4.9]	1525	3.5 ± 0.2	7.7 ± 1.1	2175	3.5 ± 0.5	7.6 ± 1.2
885	*209 ± 35*	[5.0]	1535	4.2 ± 0.2	8.5 ± 1.2	2185	3.4 ± 0.6	7.5 ± 1.2
895	(187)	[5.0]	1545	4.9 ± 0.3	9.2 ± 1.3	2195	4.5 ± 0.9	8.7 ± 1.5
905	*183 ± 31*	[5.1]	1555	6.2 ± 0.3	10.5 ± 1.5	2205	3.9 ± 0.7	8.1 ± 1.4
915	(170)	[5.2]	1565	7.4 ± 0.3	11.8 ± 1.7	2215	5.9 ± 1.3	10.2 ± 2.0
925	*171 ± 29*	[5.3]	1575	6.9 ± 0.4	11.3 ± 1.6	2225	3.8 ± 0.8	8.0 ± 1.4
935	(155)	[5.3]	1585	6.3 ± 0.3	10.7 ± 1.5	2235	2.8 ± 0.6	6.9 ± 1.2
945	*142 ± 24*	[5.2]	1595	6.3 ± 0.3	10.6 ± 1.5	2245	3.0 ± 0.8	7.1 ± 1.3
955	(140)	[5.2]	1605	5.6 ± 0.2	10.0 ± 1.4	2255	4.5 ± 0.9	8.7 ± 1.6
965	*145 ± 25*	[5.2]	1615	5.5 ± 0.2	9.8 ± 1.4	2265	(3.7)	(7.9)
975	(127)	[5.2]	1625	5.4 ± 0.2	9.7 ± 1.4	2275	3.0 ± 0.3	7.1 ± 1.1
985	*128 ± 22*	[5.3]	1635	5.7 ± 0.3	10.0 ± 1.4	2285	2.9 ± 0.5	7.0 ± 1.2
995	(114)	[5.5]	1645	5.4 ± 0.2	9.7 ± 1.4	2295	(2.7)	(6.8)
1005	(108)	[5.8]	1655	4.7 ± 0.2	9.0 ± 1.3	2305	(2.6)	(6.7)
1015	(103)	[6.0]	1665	4.0 ± 0.2	8.2 ± 1.2	2315	2.5 ± 0.3	6.6 ± 1.0
1025	(97.6)	[6.2]	1675	3.3 ± 0.1	7.5 ± 1.1	2325	4.0 ± 0.8	8.2 ± 1.4
1035	(92.4)	[6.3]	1685	3.2 ± 0.1	7.4 ± 1.1	2335	[3.3]	[7.4]
1045	(87.5)	[6.4]	1695	3.2 ± 0.1	7.3 ± 1.1	2345	[3.5]	[7.6]
1055	(82.7)	[6.4]	1705	3.7 ± 0.1	7.9 ± 1.1	2355	[3.6]	[7.7]
1065	(78.2)	[6.6]	1715	4.5 ± 0.2	8.7 ± 1.2	2365	[3.4]	[7.6]
1075	(73.9)	[7.3]	1725	5.3 ± 0.2	9.6 ± 1.3	2375	[3.2]	[7.4]
1085	(69.7)	[8.3]	1735	6.3 ± 0.3	10.7 ± 1.5	2385	[3.1]	[7.2]
1095	(65.8)	[9.1]	1745	6.7 ± 0.3	11.1 ± 1.6	2395	[2.9]	[7.0]
1105	(62.0)	[10.2]	1755	6.2 ± 0.3	10.6 ± 1.5	2405	[2.8]	[6.9]
1115	(58.4)	[11.4]	1765	6.1 ± 0.2	10.5 ± 1.5	2415	[2.8]	[6.9]
1125	(55.0)	[12.3]	1775	5.4 ± 0.2	9.7 ± 1.4	2425	[2.8]	[6.9]
1135	(51.8)	[12.7]	1785	4.8 ± 0.2	9.1 ± 1.3	2435	[2.7]	[6.8]
1145	(48.7)	[13.3]	1795	4.6 ± 0.1	8.8 ± 1.2	2445	[2.7]	[6.7]
1155	(45.7)	[13.8]	1805	4.1 ± 0.1	8.3 ± 1.2	2455	[2.6]	[6.7]
1165	(43.0)	[14.7]	1815	3.7 ± 0.1	7.9 ± 1.1	2465	[2.7]	[6.8]
1175	(40.3)	[15.6]	1825	3.6 ± 0.1	7.8 ± 1.1	2475	[2.6]	[6.7]
1185	30.6 ± 10.7[e]	[16.2]	1835	3.5 ± 0.1	7.6 ± 1.1	2485	[2.7]	[6.8]
1195	(35.4)	[16.5]	1845	3.8 ± 0.1	7.9 ± 1.1	2495	[2.8]	[6.9]
1205	(33.2)	[16.3]	1855	4.1 ± 0.2	8.3 ± 1.2	2505	[3.0]	[7.2]
1215	(31.1)	[15.7]	1865	4.9 ± 0.2	9.2 ± 1.3	2515	[3.4]	[7.5]
1225	(29.1)	[14.9]	1875	5.4 ± 0.2	9.7 ± 1.4	2525	[3.6]	[7.8]
1235	(27.2)	[14.8]	1885	5.6 ± 0.3	9.9 ± 1.4	2535	[3.5]	[7.7]
1245	(25.4)	[15.2]	1895	5.0 ± 0.3	9.2 ± 1.3	2545	[3.4]	[7.5]
1255	28.1 ± 8.6	[15.9]	1905	4.3 ± 0.2	8.5 ± 1.2	2555	[3.3]	[7.4]
1265	28.5 ± 9.3	[16.3]	1915	3.6 ± 0.2	7.7 ± 1.1	2565	[2.8]	[6.9]
1275	28.0 ± 8.6	[16.2]	1925	3.2 ± 0.2	7.3 ± 1.1	2575	[2.5]	[6.6]
1285	(19.3)	[15.8]	1935	3.3 ± 0.2	7.4 ± 1.1	2585	[2.4]	[6.5]
1295	14.6 ± 3.0	[14.9]	1945	3.4 ± 0.2	7.6 ± 1.1	2595	[2.3]	[6.3]
1305	17.6 ± 5.2	[14.3]	1955	3.7 ± 0.2	7.9 ± 1.1	2605	[1.9]	[5.9]
1315	10.1 ± 1.2	[14.0]	1965	4.6 ± 0.2	8.8 ± 1.2	2615	[1.9]	[5.9]
1325	(11.2)	[13.9]	1975	5.4 ± 0.3	9.7 ± 1.4	2625	[1.8]	[5.8]
1335	12.4 ± 2.8	[14.1]	1985	5.5 ± 0.5	9.8 ± 1.5	2635	[1.9]	[5.9]
1345	16.2 ± 4.5	[14.5]	1995	6.3 ± 0.5	10.7 ± 1.5	2645	[1.9]	[5.9]
1355	17.3 ± 5.1	[14.7]	2005	7.4 ± 0.8	11.8 ± 1.8	2655	[1.9]	[5.9]
1365	8.9 ± 1.1	13.5 ± 2.2[f]	2015	10.5 ± 2.1	15.2 ± 3.1	2665	[1.7]	[5.7]
1375	10.1 ± 1.1	14.7 ± 2.4	2025	10.2 ± 1.7	14.9 ± 2.8	2675	[1.6]	[5.6]
1385	7.8 ± 1.0	12.3 ± 2.0	2035	16.3 ± 5.0	21.4 ± 6.2	2685	[1.4]	[5.4]
1395	6.9 ± 0.7	11.3 ± 1.7	2045	17.5 ± 5.2	22.8 ± 6.5	2695	[1.3]	[5.3]
1405	7.5 ± 0.8	11.9 ± 1.9	2055	15.7 ± 2.6	20.8 ± 4.1			
1415	(7.2)	(11.7)	2065	17.9 ± 2.6	23.2 ± 4.4			
1425	7.0 ± 0.7	11.4 ± 1.7	2075	16.3 ± 4.6	21.4 ± 5.8			
1435	7.1 ± 0.7	11.5 ± 1.7	2085	10.6 ± 1.7	15.3 ± 2.8			
1445	4.9 ± 0.7	9.2 ± 1.5	2095	6.9 ± 0.6	11.3 ± 1.7			

[a]For wavelengths λ between 300 and 600 nm, the effective scattering coefficient is given by $b_e(\lambda[nm]) = (\lambda/400)^{-0.9} b_e(400)$ and absorptivity is given by $a(\lambda[nm]) = (\lambda/400)^{-1.08} a_{dust}(400) + 7 \times 10^3 e^{-6600/\lambda}$.

[b]Values in parentheses are estimates from interpolations and extrapolations of in situ optical measurements.

[c]Values in square brackets are estimates from extrapolations of ice core dust measurements.

[d]Values in italics are measurements by *Askebjer et al.* [1997b] and include a 17% systematic uncertainty.

[e]Values of $b_e(400)$ with errors are from in situ measurements with AMANDA.

[f]Values of $a_{dust}(400)$ with errors were calculated via the empirical correlation $C_{dust}[m^{-1}] = (71 \pm 12) b_e(400)[m^{-1}] + (2.6 \pm 0.6)$.

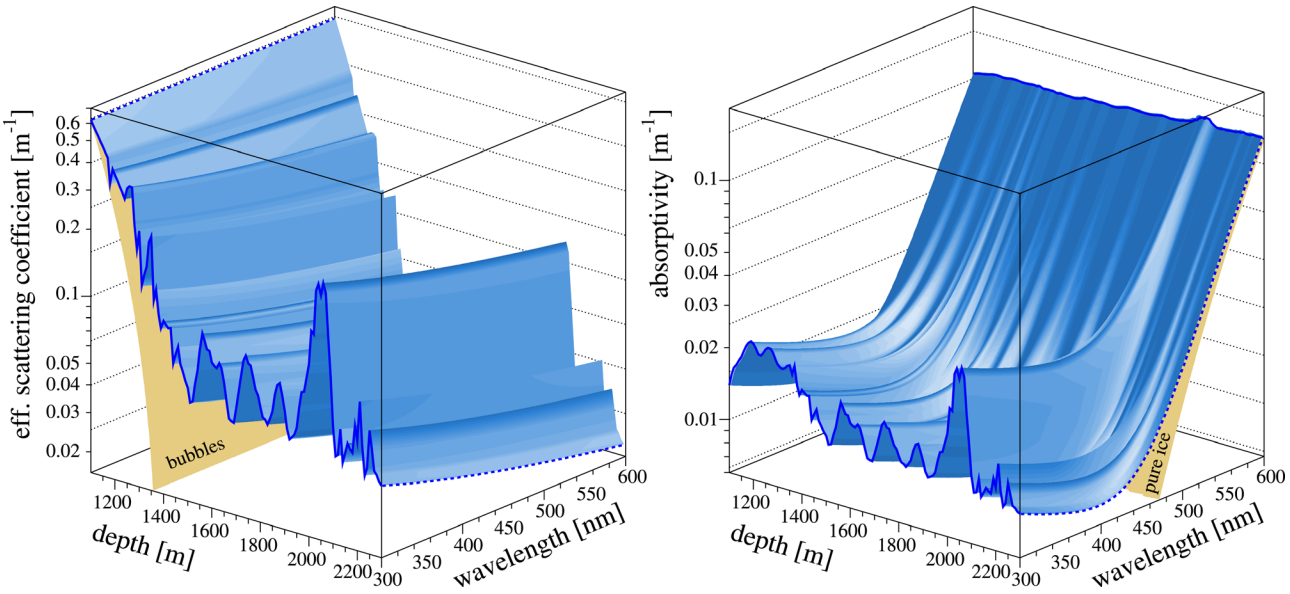

Figure 22. Maps of optical scattering and absorption for deep South Pole ice. The depth dependence between 1100 and 2300 m and the wavelength dependence between 300 and 600 nm (left) for the effective scattering coefficient and (right) for absorptivity are shown as shaded surfaces, with the bubble contribution to scattering and the pure ice contribution to absorption superimposed as (partially obscured) steeply sloping surfaces. The dashed lines at 2300 m show the wavelength dependences: a power law due to dust for scattering and a sum of two components (a power law due to dust and an exponential due to ice) for absorption. The dashed line for scattering at 1100 m shows how scattering on bubbles is independent of wavelength. The slope in the solid line for absorptivity at 600 nm is caused by the temperature dependence of intrinsic ice absorption.

correlation between C_{dust} and the contribution from dust to $b_e(400)$, were used to derive the dust profile for absorption (Figure 21, right) from the dust profile for scattering (Figure 21, left). The third parameter in our model, α, is used to calculate scattering at any wavelength from $b_e(400)$ via a power law:

$$b_e(\lambda[\mathrm{nm}]) = (\lambda/400)^{-\alpha} b_e(400). \tag{25}$$

The remaining three parameters (κ, A_{IR}, and λ_0) are used to calculate absorptivity from $a_{\mathrm{dust}}(400)$ through the two-component model:

$$a(\lambda[\mathrm{nm}]) = (\lambda/400)^{-\kappa} a_{\mathrm{dust}}(400) + A_{\mathrm{IR}} e^{-\lambda_0/\lambda}. \tag{26}$$

Maps of effective scattering coefficient and absorptivity, generated from our model and summarizing our knowledge of optical properties of South Pole ice, are shown in Figure 22 for depths between 1100 and 2300 m.

[79] Our measurements of depth dependences of the optical properties had a resolution of on the order of ten meters, and our methods probed up to two hundred meters of ice between emitter and receiver. The techniques used in this work could not resolve individual dust layers much thinner than ten meters, such as highly absorbing layers of ash deposited by volcanic eruptions. Such thin ash layers may affect the performance of AMANDA and IceCube as neutrino telescopes. Building on the remote sensing techniques presented here, a dust logger [*Miočinović et al.*, 2001; *Bay et al.*, 2001] was developed and used in both Antarctic and Greenland boreholes, where it was able to resolve centimeter-thick layers of volcanic ash. Analysis of data from a dust logger operated in the first hot-water-drilled IceCube hole confirmed that ash layers are also present in South Pole ice and can be detected with the logger technique [*Bramall et al.*, 2005]. However, the South Pole ash layers are weaker and less numerous than those detected at Siple Dome (West Antarctica) [*Bay et al.*, 2004], which is partly explained by the higher altitude of the South Pole and greater distance from Antarctic volcanoes. Highly absorbing ash layers will affect light propagation, mainly by localized depletion of photons traveling at an acute angle relative to a layer, which modifies the angular dependence of the photon yield. Scattering in thin ash layers should be similar to scattering by dust and the effect on timing should be small. Furthermore, unambiguous identification of ash layers in the depth profiles at boreholes up to one kilometer apart in the IceCube array would make it possible to measure deviations of optical properties from the horizontal. In the present analysis, we assumed that the dust structure is horizontal over the length scale probed and within the sensitivity of the measurements. However, isochronal maps made with deeply penetrating radar at the South Pole [*Blankenship and the Instrument Definition Team for a Europa Radar Sounder*, 2001] show that dust layers can tilt by up to 50 m over a square kilometer. Given the strong fluctuations in optical properties over such a depth scale, tilting dust layers would strongly affect IceCube performance and must be fully mapped. This could be achieved by using dust loggers in several widely spaced boreholes along the perimeter of the array and matching up features in

the dust profiles. For the IceCube array, whose strings reach down to 2450 m, the optical properties have to be mapped down to at least 2600 m for the simulation of neutrino-induced events. Using 405 nm LED flashers installed in every IceCube optical module, scattering and absorption can be measured with the techniques presented here for depths between 2100 m (below which AMANDA data become sparse) and 2450 m. Below this depth, a dust logger can be used to measure dust concentration with subcentimeter resolution and the optical properties can then be extrapolated on the basis of this profile. The payoff of an improved knowledge and three-dimensional spatial mapping of optical properties of deep South Pole ice will be a higher accuracy in tracking of neutrinos with ultrahigh energies back to distant astrophysical sources.

[80] **Acknowledgments.** We thank past members of the AMANDA collaboration who were instrumental in the design and deployment of light sources and in the collection of data. In particular, we thank Austin Richards who led the design and construction of the steady light sources and the nitrogen lasers. This research was supported in part by National Science Foundation grants PHY-9971390 and PHY-0203111.

References

Ackermann, M., et al. (2006), The ICECUBE prototype string in AMANDA, *Nucl. Instrum. Methods Phys. Res., Sect. A*, *556*, 169–181.

Ahrens, J., et al. (2004a), Sensitivity of the IceCube detector to astrophysical sources of high energy muon neutrinos, *Astropart. Phys.*, *20*, 507–532.

Ahrens, J., et al. (2004b), Muon track reconstruction and data selection techniques in AMANDA, *Nucl. Instrum. Methods Phys. Res., Sect. A*, *524*, 169–194.

Andrés, E., et al. (2001), Observation of high-energy neutrinos using Cherenkov detectors embedded deep in Antarctic ice, *Nature*, *410*, 441–443.

Askebjer, P., et al. (1995), Optical properties of the South Pole ice at depths between 0.8 and 1 kilometer, *Science*, *267*, 1147–1150.

Askebjer, P., et al. (1997a), Optical properties of deep ice at the South Pole: Absorption, *Appl. Opt.*, *36*, 4168–4180.

Askebjer, P., et al. (1997b), UV and optical light transmission properties in deep ice at the South Pole, *Geophys. Res. Lett.*, *24*, 1355–1358.

Barkov, N. I., and V. Y. Lipenkov (1984), *Mater. Glyatsiol. Issled.*, *51*, 178–186.

Bay, R. C., P. B. Price, G. D. Clow, and A. J. Gow (2001), Climate logging with a new rapid optical technique at Siple Dome, *Geophys. Res. Lett.*, *28*, 4635–4638.

Bay, R. C., N. Bramall, and P. B. Price (2004), Bipolar correlation of volcanism with millennial climate change, *Proc. Natl. Acad. Sci. U. S. A.*, *101*, 6341–6345.

Blankenship, D. D., and the Instrument Definition Team for a Europa Radar Sounder (2001), Subsurface evaluation of European ice-ocean interchange processes, using an orbiting ice penetrating radar, *Proc. Lunar Planet. Sci. Conf.*, *32*, Abstract 1854.

Bohren, C. F., and D. R. Huffman (1983), *Absorption and Scattering of Light by Small Particles*, John Wiley, Hoboken, N. J.

Bramall, N. E., R. C. Bay, K. Woschnagg, R. A. Rohde, and P. B. Price (2005), A deep high-resolution optical log of dust, ash, and stratigraphy in South Pole glacial ice, *Geophys. Res. Lett.*, *32*, L21815, doi:10.1029/2005GL024236.

Chandrasekhar, S. (1950), *Radiative Transfer*, 393 pp., Clarendon, Oxford, U. K.

Delmonte, B., J. R. Petit, and V. Maggi (2002), Glacial to Holocene implications of the new 27000-year dust record from the EPICA Dome C (East Antarctica) ice core, *Clim. Dyn.*, *18*, 647–660.

Grenfell, T. C., and D. K. Perovich (1981), Radiation absorption coefficients of polycrystalline ice from 400–1400 nm, *J. Geophys. Res.*, *86*, 7447–7450.

He, Y. D., and P. B. Price (1998), Remote sensing of dust in deep ice at the South Pole, *J. Geophys. Res.*, *103*, 17,041–17,056.

Henyey, L. G., and J. L. Greenstein (1941), Diffuse radiation in the galaxy, *Astrophys. J.*, *93*, 70–83.

Hoffman, P. F., A. J. Kaufman, G. P. Halverson, and D. P. Schrag (1998), A neoproterozoic Snowball Earth, *Science*, *281*, 1342–1346.

Kirk, J. T. O. (1999), Multiple scattering of a photon flux: Implications for the integral average cosine of the underwater light yield, *Appl. Opt.*, *38*, 3134–3140.

Lipenkov, V. Y. (2000), Air bubbles and air-hydrate crystals in the Vostok ice core, in *Physics of Ice Core Records*, edited by T. Hondoh, pp. 327–358, Hokkaido Univ. Press, Sapporo, Japan.

Mie, G. (1908), Beiträge zur Optik trüber Medien, speziell kolloidaler Metallösungen, *Ann. Phys. Leipzig*, *25*, 377–445.

Miller, S. L. (1969), Clathrate hydrates of air in Antarctic ice, *Science*, *165*, 489–490.

Minton, A. P. (1971), The far-ultraviolet spectrum of ice, *J. Phys. Chem.*, *75*, 1162–1164.

Miočinović, P., P. B. Price, and R. C. Bay (2001), Rapid optical method for logging dust concentration versus depth in glacial ice, *Appl. Opt.*, *40*, 2515–2521.

Perovich, D. K. (2001), Ultraviolet radiation and the optical properties of sea ice and snow, in *UV Radiation and Arctic Ecosystems*, *Ecol. Stud.*, vol. 153, edited by D. Hessen, pp. 73–89, Springer, New York.

Perovich, D. K., and J. W. Govoni (1991), Absorption coefficients of ice from 250 to 400 nm, *Geophys. Res. Lett.*, *18*, 1233–1235.

Petit, J. R., et al. (1999), Climate and atmospheric history of the past 420,000 years from the Vostok ice core, Antarctica, *Nature*, *399*, 429–436.

Price, P. B. (1995), Kinetics of conversion of air bubbles to air hydrate crystals in Antarctic ice, *Science*, *267*, 1802–1804.

Price, P. B. (2006), Attenuation of acoustic waves in glacial ice and salt domes, *J. Geophys. Res.*, *111*, B02201, doi:10.1029/2005JB003903.

Price, P. B., and L. Bergström (1997a), Enhanced Rayleigh scattering as a signature of nanoscale defects in highly transparent solids, *Philos. Mag. A*, *75*, 1383–1390.

Price, P. B., and L. Bergström (1997b), Optical properties of deep ice at the South Pole: Scattering, *Appl. Opt.*, *36*, 4181–4194.

Price, P. B., and K. Woschnagg (2001), Role of group and phase velocity in high-energy neutrino observatories, *Astropart. Phys.*, *15*, 97–100.

Price, P. B., K. Woschnagg, and D. Chirkin (2000), Age vs depth of glacial ice at South Pole, *Geophys. Res. Lett.*, *27*(14), 2129–2132.

Price, P. B., O. V. Nagornov, R. C. Bay, D. Chirkin, P. Miočinović, A. Richards, K. Woschnagg, B. Koci, and V. Zagorodnov (2002), Temperature profile for glacial ice at the South Pole: Implications for life in a nearby subglacial lake, *Proc. Natl. Acad. Sci. U. S. A.*, *99*, 7844–7847.

Ruth, U., D. Wagenbach, J. P. Steffensen, and M. Bigler (2003), Continuous record of microparticle concentration and size distribution in the central Greenland NGRIP ice core during the last glacial period, *J. Geophys. Res.*, *108*(D3), 4098, doi:10.1029/2002JD002376.

Sauberer, F. (1950), Die spektrale Strahlungsdurchlässigkeit des Eises, *Wetter Leben*, *2*, 193–197.

Trodahl, H. J., and R. G. Buckley (1990), Enhanced ultraviolet transmission of Antarctic sea ice during the Austral spring, *Geophys. Res. Lett.*, *17*, 2177–2179.

Uchida, T., W. Shimada, T. Hondoh, S. Mae, and N. I. Barkov (1995), Refractive-index measurements of natural air-hydrate crystals in an Antarctic ice sheet, *Appl. Opt.*, *34*, 5746–5749.

Urbach, F. (1953), The long-wavelength edge of photographic sensitivity and of the electronic absorption of solids, *Phys. Rev.*, *92*, 1324.

Warren, S. G. (1984), Optical constants of ice from the ultraviolet to the microwave, *Appl. Opt.*, *23*, 1206–1225.

Warren, S. G., R. E. Brandt, T. C. Grenfell, and C. P. McKay (2002), Snowball Earth: Ice thickness on the tropical ocean, *J. Geophys. Res.*, *107*(C10), 3167, doi:10.1029/2001JC001123.

Watanabe, O., K. Kamiyama, H. Motoyama, Y. Fujii, H. Shoji, and K. Satow (1999), The paleoclimate record in the ice core from Dome Fuji station, Antarctica, *Ann. Glaciol.*, *29*, 176–178.

Woschnagg, K., and P. B. Price (2001), Temperature dependence of absorption in ice at 532 nm, *Appl. Opt.*, *40*, 2496–2500.

M. Ackermann, E. Bernardini, S. Böser, M. Kowalski, R. Lang, H. Leich, M. Leuthold, R. Nahnhauer, E. Resconi, S. Schlenstedt, C. Spiering, P. Steffen, K.-H. Sulanke, O. Tarasova, M. Walter, R. Wischnewski, and H. Wissing, Deutsches Elektronen-Synchrotron, D-15738 Zeuthen, Germany.

J. Ahrens, T. Becka, T. Feser, M. Hellwig, L. Köpke, T. Neunhöffer, and H.-G. Sander, Institute of Physics, University of Mainz, D-55099 Mainz, Germany.

X. Bai, T. K. Gaisser, T. Hauschildt, P. Niessen, and S. Tilav, Bartol Research Institute, University of Delaware, Newark, DE 19716, USA.

M. Bartelt, J. K. Becker, A. Groß, T. Messarius, K. Münich, W. Rhode, and W. Wagner, Institute of Physics, University of Dortmund, D-44221 Dortmund, Germany.

S. W. Barwick, L. Gerhardt, K. Kuehn, J. W. Nam, and A. Silvestri, Department of Physics and Astronomy, University of California, Irvine, CA 92717, USA.

R. C. Bay, D. H. Hardtke, P. Miočinović, R. Porrata, P. B. Price, M. Solarz, I. Taboada, and K. Woschnagg (corresponding author), Department of Physics, University of California, Berkeley, CA 94720, USA. (kurtw@berkeley.edu)

K.-H. Becker, H. Geenen, T. Harenberg, K. H. Kampert, and C. H. Wiebusch, Department of Physics, University of Wuppertal, D-42097 Wuppertal, Germany.

P. Berghaus, D. Bertrand, and O. Bouhali, Science Faculty CP230, Université Libre de Bruxelles, B-1050 Brussels, Belgium.

D. J. Boersma, J. Cooley, P. Desiati, R. Ganugapati, F. Halzen, K. Hanson, G. C. Hill, J. Hodges, B. Hughey, A. Karle, R. Morse, K. Rawlins, S. Richter, D. Schneider, R. Schwarz, M. Stamatikos, D. Steele, and Y.-R. Wang, Department of Physics, University of Wisconsin, Madison, WI 53706, USA.

O. Botner, A. Bouchta, J. Conrad, A. Davour, C. P. de los Heros, A. Hallgren, J. Lundberg, P. Marciniewski, and A. C. Pohl, Division of High Energy Physics, Uppsala University, SE-75121 Uppsala, Sweden.

C. Burgess, T. Burgess, P. Ekström, P. O. Hulth, K. Hultqvist, S. Hundertmark, Y. Minaeva, J. Rodríguez Martino, L. Thollander, and C. Walck, Department of Physics, Stockholm University, SE-10691 Stockholm, Sweden.

T. Castermans, P. Herquet, G. Kohnen, and M. Ribordy, Faculty of Sciences, University of Mons-Hainaut, B-7000 Mons, Belgium.

D. Chirkin, A. Goldschmidt, K. Helbing, J. Jacobsen, H. S. Matis, C. P. McParland, D. R. Nygren, G. T. Przybylski, and R. G. Stokstad, Lawrence Berkeley National Laboratory, Berkeley, CA 94720, USA.

B. Collin, D. F. Cowen, T. DeYoung, and M. Kestel, Department of Physics and Astronomy, Pennsylvania State University, University Park, PA 16802, USA.

C. De Clercq, D. Hubert, and P. Olbrechts, Dienst ELEM, Vrije Universiteit Brussel, B-1050 Brussels, Belgium.

I. Liubarsky, Blackett Laboratory, Imperial College, London SW7 2BZ, UK.

J. Madsen and G. M. Spiczak, Department of Physics, University of Wisconsin, River Falls, WI 54022, USA.